OPEN ACCESS



Discovery of a Dense Association of Stars in the Vicinity of the Supermassive Black Hole Sgr A*

S. Elaheh Hosseini^{1,2}, Andreas Eckart^{1,2}, Michal Zajaček^{3,1}, Silke Britzen², Harshitha K. Bhat^{1,2}, and Vladimír Karas⁴

¹ I. Physikalisches Institut der Universität zu Köln, Zülpicher Str. 77, D-50937 Köln, Germany ² Max-Planck-Institut für Radioastronomie (MPIfR), Auf dem Hügel 69, D-53121 Bonn, Germany ³ Department of Theoretical Physics and Astrophysics, Faculty of Science, Masaryk University, Kotlářská 2, 611 37 Brno, Czech Republic ⁴ Astronomical Institute of the Czech Academy of Sciences, Boční II 1401, CZ-141 00 Prague, Czech Republic Received 2022 November 10; revised 2024 September 2; accepted 2024 September 17; published 2024 November 7

Abstract

We focus on a sample of 42 sources in the vicinity of the bow-shock source IRS 1W (N-source region), located at a distance of 6."05 northeast of the supermassive black hole Sagittarius A* (Sgr A*), within the radius of 1."35. We present the first proper-motion measurements of N sources and find that a larger subset of N sources (28 sources) exhibit a north-west (NW) flying angle. These sources can be bound by an intermediate-mass black hole (IMBH) or the concentration that we observe is due to a disk-like distribution projection along the line of sight. We detect the N sources in the H, K_s , and L' bands. The NW-ward flying sources could be a bound collection of stars. We discuss the tentative existence of an IMBH or an inclined disk distribution to explain the significant overdensity of stars. The first scenario of having an IMBH implies the lower limit of $\sim 10^4 \, M_\odot$ for the putative IMBH. Our measurements for the first time reveal that the dense association of stars containing IRS 1W is a comoving group of massive, young stars. This stellar association might be the remnant core of a massive stellar cluster that is currently being tidally stripped as it inspirals toward Sgr A*. The second scenario suggests that the appearance of the N sources might be influenced by the projection of a disk-like distribution of younger He-stars and/or dust-enshrouded stars.

Unified Astronomy Thesaurus concepts: Galactic center (565); Stellar associations (1582); Young star clusters (1833); Intermediate-mass black holes (816); Infrared astronomy (786); Infrared photometry (792); Proper motions (1295); Stellar motion (1615); Star clusters (1567); Stellar kinematics (1608); Astrophysical black holes (98); Infrared excess (788)

1. Introduction

The extended radio source Sgr A consists of three components in terms of different radiative and spatial properties: Sgr A East, which is a nonthermal supernova remnant, Sgr A West, which is a thermal region associated with the ionized minispiral structure, and the compact variable radio source Sgr A* associated with the supermassive black hole (SMBH) of $\sim 4 \times 10^6 M_{\odot}$ (B. Balick & R. L. Brown 1974; A. Eckart & R. Genzel 1996; W. M. Goss & R. X. McGee 1996; A. M. Ghez et al. 1998; R. Genzel et al. 2010, 2024; A. Eckart et al. 2017; GRAVITY Collaboration et al. 2019a; E. H. T. Collaboration et al. 2022, and references therein) at the center of the Milky Way. The thermal Sgr A West region or the minispiral (K. Y. Lo & M. J. Claussen 1983; R. D. Ekers et al. 1983) is detected as a distinct filamentary structure in near- and mid-infrared bands (Y. Clénet et al. 2004; T. Viehmann et al. 2006; K. Mužić et al. 2007; H. K. Bhat et al. 2022) as well as in the millimeter and radio domain (J.-H. Zhao et al. 2009, 2010; L. Moser et al. 2017). It is composed of three clumpy streamers orbiting around Sgr A* that consist of dust and ionized and atomic gas with a dust temperature of ~100 K and a gas temperature of $\sim 10^4$ K (F. Yusef-Zadeh et al. 1998; D. Kunneriath et al. 2012).

A surprisingly large number of massive young stars with the age of a few million years resides in the Milky Way's

Original content from this work may be used under the terms of the Creative Commons Attribution 4.0 licence. Any further distribution of this work must maintain attribution to the author(s) and the title of the work, journal citation and DOI.

innermost half parsec. They form at least one disk-like structure of clockwise (CW) orbiting stars (R. Genzel et al. 2003; Y. Levin & A. M. Beloborodov 2003). T. Paumard et al. (2006) also propose the existence of a second disk of counterclockwise (CCW) orbiting stars, which, however, appears to be less populous. The existence of disk-like structures, which can be traced even within the innermost S cluster (B. Ali et al. 2020), suggests the association of star formation in the Galactic center (GC) with the accretion disks that formed during the previous enhanced accretion activity of Sgr A*.

The mechanism that leads to the presence of young stars with the age of \lesssim 5 Myr is still not completely understood because there are several factors in the Galactic center environment that should be inhibiting the star formation process, such as intense UV radiation and stellar winds, large turbulence, enhanced magnetic field, and the tidal forces from the SMBH (M. Morris 1993). This problem is known as the "paradox of youth" (A. M. Ghez et al. 2003), though with the advancements in star formation and dynamical models in galactic nuclei, it has been possible to explain the occurrence of young stars in the Galactic center (see, e.g., M. Mapelli & A. Gualandris 2016, for a review).

Three plausible scenarios are generally discussed:

 An in situ star formation approach, in which stars form in the gravitationally unstable accretion disk or within an infalling molecular cloud that gets shocked due to collisions with the surrounding gas or is tidally compressed (M. Morris 1993; Y. Levin & A. M. Beloborodov 2003; S. Nayakshin et al. 2006; T. Paumard et al. 2006;

- H. Bartko et al. 2009; A. Hobbs & S. Nayakshin 2009; J. R. Lu et al. 2009; H. Bartko et al. 2010; B. Jalali et al. 2014).
- 2. An inspiral star formation approach, which claims that the star cluster first starts forming outside the central parsec, e.g., within the circumnuclear disk (CND) or even further away in the central molecular zone. The presence of an intermediate-mass black hole (IMBH) can shorten the dynamical friction timescale, which needs to be at most a few million years long in order for stars to be still young when they settle around the SMBH (O. Gerhard 2001; B. M. S. Hansen & M. Milosavljević 2003; S. L. W. McMillan & S. F. Portegies Zwart 2003; S. J. Berukoff & B. M. S. Hansen 2006; S. F. Portegies Zwart et al. 2006; F. P. Rizzuto et al. 2021; F. Peißker et al. 2021).
- 3. A rejuvenation scenario, which proposes that late-type stars have undergone collisions with other stars, a dense accretion disk, or a jet, which caused their colder outer layers to be stripped off and made them appear hotter and younger than they actually would be (M. Morris 1992, 1993; R. Genzel et al. 2003; M. Zajaček et al. 2020). In addition, late-type stars aligned with an accretion disk accrete material from it, which also leads to their rejuvenation by gaining fresh hydrogen (M. Cantiello et al. 2021).

Apart from the cluster of young stars centered around Sgr A* within ~ 0.5 pc, there is a distinct concentration of infrared sources, IRS 13, located at the projected distance of $\sim 3''-4''$ $(\sim 0.12-0.16 \,\mathrm{pc})$ southwest of Sgr A* (F. Peißker et al. 2023, 2024; C. K. Dinh et al. 2024). IRS 13 has been studied as a suitable candidate for the first two aforementioned scenarios for the origin of young stars in the central parsec. IRS 13 consists of two components—the northern part, IRS 13N, and the eastern part, IRS 13E. IRS 13N hosts young, infraredexcess sources (A. Eckart et al. 2004, 2013; J. P. Maillard et al. 2004; T. Paumard et al. 2006; K. Mužić et al. 2008). IRS 13E mainly contains massive Wolf-Rayet (W-R) stars and the violent supergiant E1(OBI) (J. P. Maillard et al. 2004; J. Moultaka et al. 2005; T. Paumard et al. 2006), whereas the rest of the stars are fainter ones, identified as late-type stars and are most likely the background stars (T. K. Fritz et al. 2010).

The velocity dispersion of the IRS 13E sources motivated the speculation about the existence of an IMBH to bind the cluster and thus prevent it from tidal disruption at the given distance from Sgr A*. The required mass of the assumed IMBH was inferred to be about $\sim 10^4 M_{\odot}$ (J. P. Maillard et al. 2004; R. Schödel et al. 2005). The existence of the prominent X-ray source in the IRS 13E cluster reinforced the discussion about the IMBH. On the other hand, Z. Zhu et al. (2020) argue that a colliding wind scenario between E2 and E4 can explain the X-ray spectrum as well as the morphology of IRS 13E and suggests that there is no significant evidence that IRS 13E hosts an IMBH more massive than $\sim 10^3~M_{\odot}$. In general, the occurrence of IMBHs in nuclear star clusters is expected based on dynamical arguments. S. C. Rose et al. (2022) propose that dynamical mechanisms operating in galactic nuclei, specifically black hole-star collisions, mass segregation, and relaxation, are particularly effective in the formation of IMBHs of $\lesssim 10^4 M_{\odot}$. Their findings imply that at least one IMBH is likely to exist in the central parsec of the Galaxy. Another channel for the occurrence of IMBHs in galactic nuclei is their infall within

massive stellar clusters (L. Spitzer 1969; S. F. Portegies Zwart & S. L. W. McMillan 2002; F. A. Rasio et al. 2004; G. Fragione 2022), which directly relates dense stellar associations such as IRS 13 with an IMBH. S. C. Rose et al. (2022) suggest that the collisions between black holes and stars can contribute to the diffuse X-ray emission in the Galactic center region. Hence, also a growing black hole inside IRS 13E that collides with the surrounding stars could contribute to the X-ray emission of the cluster.

Another apparent concentration of stars in the inner parsec of the Galactic center is associated with the source IRS 1W, which is located within the northern arm of the mini-spiral. The minispiral contains mostly hot, ionized gas traced by bright Br γ emission. B. Vollmer & W. J. Duschl (2000) interpret the kinematics of the ionized gas in the northern arm to be Keplerian. IRS 1W has been studied previously as a bow-shock source interacting with the material of the northern arm. Its broadband infrared continuum emission is consistent with the temperature of $\sim \! 300 \, \mathrm{K}$ (A. Tanner et al. 2002, 2005; A. M. Tanner et al. 2003), suggesting the presence of warm dust in its bow shock.

T. Ott et al. (1999) used the speckle camera SHARP on the New Technology Telescope and showed that IRS 1W is an extended source that could be a young star. Previously, it was suggested that it could have formed in the northern arm of the mini-spiral or from the accreted gas and dust in the infalling material out of the northern arm. However, due to the current low inferred mass of the mini-spiral gas of $\sim 100 \, M_{\odot}$ it is unlikely that it formed within the northern arm. A. Tanner et al. (2005) observed IRS 1W alongside IRS 10W and IRS 21 by W.M. Keck 10 m and Gemini 8 m telescopes and identified them as bow-shock sources with central sources as W-R stars. The stellar-wind properties and kinematics of IRS 1W are similar to the properties of the CW orbiting He emission-line stars. T. Viehmann et al. (2006) showed that IRS 1W is very red and has a featureless spectral energy distribution (SED). J. Sanchez-Bermudez et al. (2014) analyzed the bow-shock orientation alongside the proper motion and confirmed that IRS 1W is a W-R star with a bow shock created by the interaction between the mass-losing star and the surrounding interstel-

The apparent stellar overabundance in the vicinity of IRS 1W could hypothetically be a stellar cluster similar to IRS 13 that is getting tidally disrupted upon the approach toward the SMBH. We investigate this possibility in more detail in this paper. We focus on the area around IRS 1W that contains 42 sources, including IRS 1W. The geometrical center of these sources is situated at 6.24 ± 0.47 (R.A.) and 0.25 ± 0.42 (decl.) with respect to Sgr A* in the 2005.366 epoch within the circular region with a radius of 1.35.

This paper is structured as follows. In Section 2, we describe analyzed data sets in the near-infrared (NIR) domain. The identification of stars associated with IRS 1W that constitute an apparent overabundance in comparison with other fields around Sgr A* is analyzed in Section 3. The NIR photometry color–color diagram of the sources is presented in Section 4. Proper motions of the sources are analyzed in Section 5, where the significant stellar concentration with the common proper motion in the north–west (NW) direction is identified. We discuss potential clustering scenarios (IMBH-bound cluster or a projected disk-like distribution) in Section 6. Finally, we summarize the main results in Section 7.

2. Observations and Data Reduction

The Galactic center observations presented in this paper are based mostly on the infrared data sets, with the addition of the data from the X-ray domain. The infrared observations were carried out using the Nasmyth Adaptive Optics System/Coude NIR Camera at the European Southern Observatory Very Large Telescope (VLT). The M-type supergiant IRS 7 located at \sim 5"5 north of Sgr A* (E. E. Becklin & G. Neugebauer 1975; M. J. Lebofsky et al. 1982; F. Yusef-Zadeh & M. Morris 1991) serves as a natural guide star for the adaptive optics system. The X-ray data was obtained using the Chandra X-Ray Observatory. The K_s -band data (2.2 μ m) were taken at Unit 4 (UT4)-YEPUN from 2002 to 2013 and from 2014 at UT1-Antu on Paranal, Chile. The K_s -band images taken with the S13 camera have a pixel scale of 13 mas pixel⁻¹ and there is one data set among our studied data sets in the K_s -band data taken by the S27 camera, which has a pixel scale of 27 mas pixel⁻¹. We use 16 epochs from 2003.451 to 2018.311 (28 observations) to derive the proper motions of a group of stars located at the east side of the bow-shock object IRS 1W in a circular region with a radius of about 1."35 (1" corresponds to 0.04 pc; hence, the region has a physical radius of \sim 54 milliparsecs).

In this work, for photometric purposes, we use the H-(1.6 μ m), K_s -(2.2 μ m) and L'-(3.8 μ m) band data obtained with the NACO@VLT with a pixel scale of 13, 13, and 27 mas pixel⁻¹, respectively, and the X-ray data with the pixel scale of 492 mas pixel⁻¹. In Table 1, we summarize all the data sets that are a part of our analysis.

The standard data reduction process is applied to all of our infrared data sets that consists of sky subtraction, flat-fielding, bad and dead pixel correction, and finally combining the images for each epoch via a shift-and-add algorithm to obtain the final array.

The X-ray data span the energy range from 0.5 to 8 keV and from 4 to 8 keV in 2005. The X-ray data reduction follows the procedure as explained in E. Mossoux & A. Eckart (2017).

3. Source Identification

We study sources within a circular region located at \sim 6."05 northeast (NE) of Sgr A* with a radius of \sim 1."35 (shown in Figure 1). In this section, we show that the circular region is not chosen arbitrarily but rather it encompasses the stellar overabundance in the region. By increasing the aperture size, the density of sources drops significantly. In addition, there is a visible gap between the N sources' region and the IRS 16 sources' region.

The brightest star in this region is the aforementioned bowshock source IRS 1W. We identify 42 sources including IRS 1W in the previously described region. We name the sources starting with the letter N from N1 for IRS 1W to N42. In Figure 2, we show the identified sources in the K_s band. We call these sources the N sources for simplicity. The N sources are not only identified in the K_s band but also in the H and L'bands.

We determined the positions of the N sources using the StarFinder software (E. Diolaiti et al. 2000) in the K_s -band high-pass-filtered images from 2003.451 to 2018.311 over 16 epochs.

When we investigate the number of the N sources with respect to the radial distance from the geometrical center of the N sources (Figure 3), we find a gradual decrease in the number

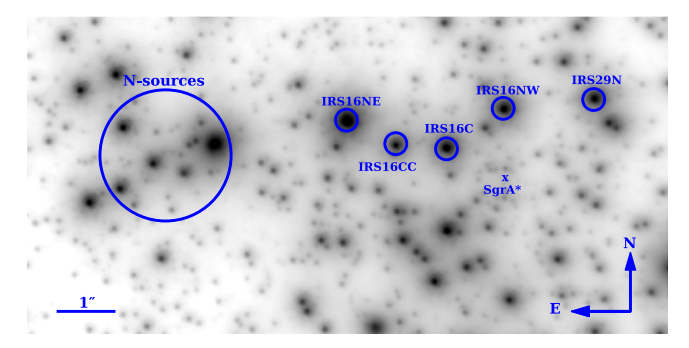


Figure 1. The image obtained in the K_s band from the 2005.366 epoch. Symbol "x" denotes the position of Sgr A*. The encircled N sources at the projected distance of $\sim 6!'05$ with respect to Sgr A* stands for the region of our study.

Table 1
Summary of NIR Observations in the H, K_s , and L' Bands, Including the Date, Camera, Filter, and Observation ID

Camera, Tiner, and Observation in					
Date	Camera	Filter	Observation ID		
2003.451	S13	K_s	713-0078(A)		
2003.453	S13	K_s	713-0078(A)		
2003.456	S13	K_s	713-0078(A)		
2003.464	S13	K_s	271.B-5019(A)		
2003.763	S13	K_s	072.B-0285(A)		
2004.518	S13	K_s	073.B-0775(A)		
2004.663	S13	K_s	073.B-0775(A)		
2004.671	S13	K_s	073.B-0775(B)		
2004.728	S13	K_s	073.B-0085(C)		
2005.270	S13	K_s	073.B-0085(I)		
2005.366	S13	K_s	073.B-0085(D)		
2005.371	S13	K_s	073.B-0085(D)		
2005.374	S13	K_s	073.B-0085(D)		
2005.467	S27	K_s	073.B-0085(F)		
2005.569	S13	K_s	075.B-0093(C)		
2005.574	S13	K_s	075.B-0093(C)		
2005.577	S13	K_s	075.B-0093(C)		
2005.585	S13	K_s	075.B-0093(C)		
2006.585	S13	K_s	077.B-0014(D)		
2007.253	S13	K_s	179.B-0261(C)		
2007.256	S13	H	179.B-0261(A)		
2009.503	S13	K_s	183.B-0100(D)		
2009.508	S13	K_s	183.B-0100(D)		
2010.240	S13	K_s	183.B-0100(L)		
2013.667	S13	K_s	091.B-0183(B)		
2017.456	S13	K_s	598.B-0043(L)		
2018.306	S13	K_s	598.B-0043(O)		
2018.311	S13	K_s	0101.B-0052(B)		
2008.400	L27	L'	081.B-0648(A)		

Note. *K_s*-band data is used for proper-motion measurements. Photometric measurements are performed in all of the corresponding bands. The pixel scale of the NACO S13 camera is 13 mas pixel⁻¹ and that of S27 is 27 mas pixel⁻¹.

of the sources with the increasing radial distance. This is an expected trend for at least a partially relaxed star cluster with a cusp-like power-law density distribution. Strong variations in source density are unlikely to be caused by the variable extinction across the field under investigation. These variations amount to a maximum of ± 0.2 in $H - K_s$ and $K_s - L$ following R. Schödel et al. (2010) over the entire field and even less across the individual regions.

To test the cluster hypothesis for the N sources, it is crucial to compare their number density with random areas distributed

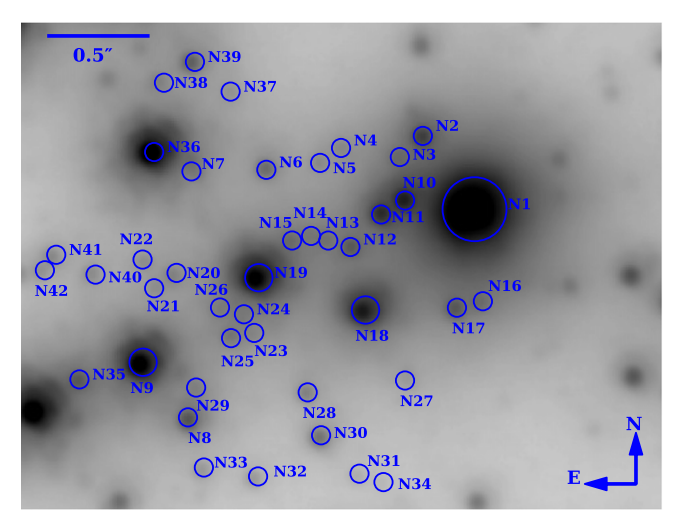


Figure 2. The K_s -band image from the 2005.366 epoch. The sources are labeled from N1/IRS 1W to N42. The figure is a zoom-in of the encircled N sources' region in Figure 1, which is located ~ 6.00000 NE of Sgr A*.

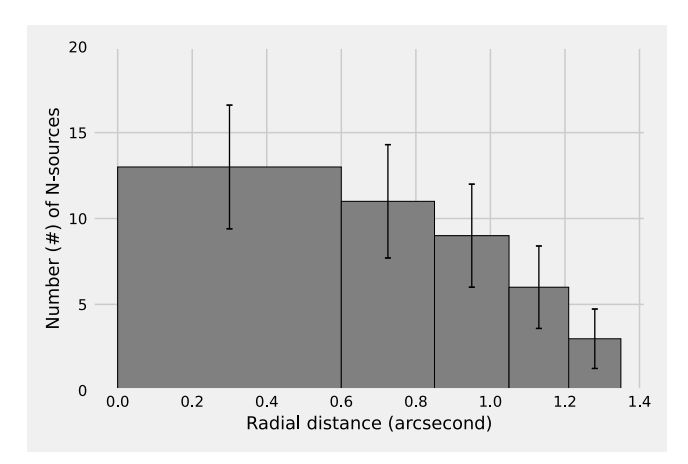


Figure 3. Distribution of N sources as a function of the projected distance with respect to the geometrical center of the association. The *y*-axis denotes the number of sources and the *x*-axis shows the radial distance (in arcseconds) from the geometrical center of N sources. The width of the bins in the histogram is defined by concentric apertures centered at the geometrical center of N sources. In addition, each annulus has an equal area to the central disk, with a radius of 0.% for the central disk, and a radial extent of 0.%6-0.%8 for the first annulus, 0.%8-1.%0 for the second annulus, 1.%0-1.%2 for the third annulus, and 1.%2-1.%3 for the fourth annulus.

isotropically at a comparable distance from Sgr A*. A stable cluster or a stellar association in the Galactic center must necessarily be characterized by an overdensity with respect to other comparable regions. To achieve this goal, we select 11 random circular regions with two conditions. First, the center of each region should have the same distance from Sgr A* as the distance of the N sources' region. Second, each of these circular regions should have the same radius as the chosen aperture representing the N-source region. These comparison regions are labeled from "Region 1" to "Region 11" as shown in the Appendix (Figure 14). The number of detected stars in the K_s band in each region is listed in Table 2. The mean number of sources in our 11 random samples is 14.6 ± 1.5 . The number of sources in our 11 regions shows that the N-source region is characterized by a significant stellar overdensity, which leads us to speculate that the N sources or their subgroup form a bound stellar association.

Aperture ID N Sources	Number of Sources 42
Region 1	15
Region 2	13
Region 3	13
Region 4	16
Region 5	16
Region 6	17
Region 7	14
Region 8	14
Region 9	12
Region 10	15
Region 11	16

Note. Each region is located at a distance of about $6\rlap.{''}05$ from Sgr A^* and its radius is $\sim 1\rlap.{''}35$. The mean number of sources in these 11 regions is 14.6 ± 1.5 .

We cross checked the identified N sources with the previous proper-motion and radial-velocity studies (R. Schödel et al. 2009; T. K. Fritz et al. 2016; S. D. von Fellenberg et al. 2022) that include stars in the N-source region. There are 13 corresponding sources in R. Schödel et al. (2009), out of which eight move northward, eight common sources in T. K. Fritz et al. (2016), out of which five share the northward direction, and five common sources in S. D. von Fellenberg et al. (2022) that all move northward. Hence, for the majority of the common sources, there is consistency in the proper motion. Differences arise mostly for fainter sources (10 times fainter than the brightest object), which are affected by larger uncertainties in the identification in the crowded field. In R. Schödel et al. (2009), the images were subjected to a pointspread function (PSF) fitting routine in order to extract the point source positions. In T. K. Fritz et al. (2016), the positions were extracted from Lucy deconvolved images (see also S. D. von Fellenberg et al. 2022, and references therein). The high-pass filtering method applied in this work is a linear process in which all image scales and distances are preserved. No PSF fitting is involved, yet the bulk of the PSF is removed and the high-resolution image cores of the stars are preserved. It is free from potential deconvolution artifacts that may occur, especially for fainter sources, in particular if the number of iterations is kept too small. It is also free from potential uncertainties that may occur if the PSF is fitted, in particular to faint sources in a crowded field. In addition, the temporal baseline in this work is 15 yr, while it is more limited in the previous works (by a factor of 2.5 longer than the baseline in R. Schödel et al. 2009).

4. Color-Color Diagram

The flux densities of N sources in the H, K_s , and L' bands are obtained using aperture photometry with an aperture radius of 4, 4, and 3 pixels in the H, K_s , and L' bands, respectively. Our reference stars for photometry are IRS 10W, IRS 21, and IRS 16NW, and their dereddened magnitudes are taken from R. D. Blum et al. (1996). In order to optimize the background subtraction for each source and reference stars, we use two apertures around the source with the same size as photometry apertures. The flux densities for Vega in the H, K_s , and L'

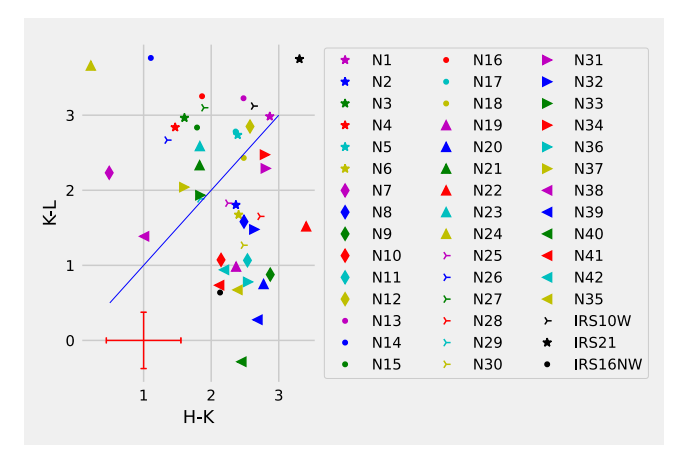


Figure 4. *HKL* two-color diagram. The solid blue line denotes the colors of a one-component blackbody at different temperatures. The red cross represents the uncertainty of the values. The red cross denotes the mean photometric uncertainties.

bands are 1050, 667, and 248 Jy, respectively. All N sources are detected in the H, K_s , and L' bands. We list their corresponding dereddened magnitudes in Table 5 and the derived color indices $H - K_s$ and $K_s - L'$ in Table 6. The results are presented in the color–color diagram, see Figure 4.

It cannot be excluded that several (e.g., four) of the bluest stars could be foreground stars. In the literature, the cut to identify foreground stars is often set around 1.3-1.8 mag (R. Schödel et al. 2010; T. K. Fritz et al. 2016). However, the foreground extinction is also variable, and on spatial scales of less than 1" typical angular resolution of the extinction maps, it cannot be excluded that these blue stars (independent of their brightness) are local cluster stars with exceptionally low foreground extinction. However, for the faint sources presented here, the stellar photometry has large uncertainties, and the bluest stars could still be consistent with being in the Galactic center—with the possible exception of N24 with a rather blue H-K value. Given these facts, we assume that the region is free of genuine foreground stars that are not part of the Galactic center nuclear stellar cluster.

An interpretation of the color–color diagram shown in Figure 4 is possible in the framework of the corresponding diagrams shown in Figure 16 of A. Eckart et al. (2013). Within the uncertainties, the sources that are located to the right of the single-component blackbody line are objects reddened by the extinction toward the Galactic center region. Objects that are located above the blackbody line experience additional local extinction due to dust locally present in or in front of the IRS 1W region.

5. Proper Motion

For the first time, we derive and present proper motions of N sources. The prevailing angle of the proper motion is northward, which suggests that N sources could be a comoving group of stars.

In order to study the proper motions of candidate stars, we identified the N sources in K_s -band images from 2003 to 2018. With the aid of the S2 star position in each epoch, the position of each source was transformed into the common coordinate system with the central position of Sgr A*. As an example, we show the best-fitting proper motions based on the derived

positions as a function of time in R.A. and decl. directions in Figure 15 for the star N2.

We adopt the distance of 8 kpc to Sgr A* (H. Shapley 1928; M. J. Reid 1993; F. Eisenhauer et al. 2003; GRAVITY Collaboration et al. 2019b) to transform the proper motions to velocities. The inferred velocities are listed in Table 3 alongside the R.A. and decl. coordinates with respect to Sgr A* for all the sources. IRS 1W, IRS 16C, IRS 16CC, IRS 16NE, and IRS 16NW are adopted as reference stars (Table 4), which show an agreement in terms of the inferred velocities with the presented values in T. Paumard et al. (2006) within uncertainties.

While the brighter sources in the overall fields show good agreement with proper-motion measurements taken from the literature (see Table 4), the predominant portion of the stars given in Table 3 have no reported data in the literature (see otherwise plentiful sets given by H. Bartko et al. 2009; S. Yelda et al. 2014; A. Feldmeier-Krause et al. 2015; S. D. von Fellenberg et al. 2022). Some of them have high velocities and may either be foreground stars or only loosely bound to the overall cluster. Here, data over a longer baseline in time and/or spectroscopy data with high sensitivity and angular resolution are required.

The velocity dispersion in R.A., corrected for the mean error of 19.0 km s⁻¹, is $\sigma_{RA} = 58.6^{+2.3}_{-1.4}$ km s⁻¹, and in decl., corrected for the mean error of 39.3 km s⁻¹, is $\sigma_{decl.} = 127.3^{+3.4}_{-1.5}$ km s⁻¹. The fact that the mean dispersion in decl. direction is larger by a factor of 2 may point to an increased source density in that direction. This would support a disk solution, as discussed later. Such a source density enhancement could manifest itself in background variations and therefore difficulties in source positioning and determination of the proper motions. However, as we show later for the NW sources, when we remove a few sources exceeding the escape velocity (these are fainter sources), the dispersion in decl. approaches the one in R.A.. The total on-sky velocity dispersion is $\sigma_{\star} = 128.0^{+4.1}_{-2.5} \,\mathrm{km \ s^{-1}}$. When we remove four sources classified as late-type stars by T. K. Fritz et al. (2016) (N6, N9, N28, and N30 with the determined line-of-sight velocities), the velocity dispersion values in R.A., decl., and the total on-sky velocity dispersion are not affected significantly and are within the values for the whole N cluster ($\sigma_{R.A.} = 59.9 \,\mathrm{km \, s}^{-1}$, $\sigma_{decl.} =$ $127.0 \,\mathrm{km \, s^{-1}}$, and $\sigma_{\star} = 122.0 \,\mathrm{km \, s^{-1}}$).

In Figure 5, we show the proper motions of the N sources superposed on a K_s -band (2.2 μ m) image. In general, these sources move toward either the NE or NW. In Figure 6, we plot the distribution of the N sources with respect to their flying angle, which indicates two distinct populations of stars. The NW-flying sources are depicted in blue, whereas the NE-flying ones are in red. The Gaussian-like distribution of the number of the NW-flying sources with respect to the flying angle supports the clustering model of these sources. On the other hand, NEflying sources exhibit a flat distribution of the number of sources with respect to the flying angle. In summary, 28 sources out of the total 42 identified N sources move NW-ward (N1, 2, 3, 4, 5, 6, 7, 9, 10, 11, 12, 15, 18, 19, 22, 23, 24, 25, 26, 27, 30, 31, 35, 36, 37, 39, 40, 42), while the rest (14 sources) move NE-ward (N8, 13, 14, 16, 17, 20, 21, 28, 29, 32, 33, 34, 38, 41). The number of NE-flying sources is consistent with the mean number in random test regions, see Table 2, which suggests that they mostly belong to the background/foreground nuclear star cluster population. The possible expectation of a broader range of angles for the random NE-flying sources that

Table 3Velocities of N Sources over the 16 yr of Monitoring

Name	$\Delta \alpha$ (arcsec)	$\Delta \delta$ (arcsec)	$V_{ m R.A.} \ ({ m km~s}^{-1})$	$V_{\rm Decl.} \ ({ m km \ s}^{-1})$	$V (\text{km s}^{-1})$	Angle (deg)
	. ,					
N1	5.15 ± 0.01	0.58 ± 0.01	-89.11 ± 16.31	349.24 ± 43.99	360.43 ± 42.81	-14.31 ± 8.56
N2	5.39 ± 0.01	0.95 ± 0.01	-72.43 ± 10.62	336.35 ± 36.78	344.06 ± 36.03	-12.15 ± 6.09
N3	5.51 ± 0.01	0.84 ± 0.01	-48.16 ± 28.06	111.11 ± 31.85	121.10 ± 31.28	-23.43 ± 35.88
N4	5.80 ± 0.01	0.89 ± 0.01	-86.84 ± 15.93	304.88 ± 27.68	317.01 ± 26.98	-15.90 ± 8.30
N5	5.91 ± 0.01	0.82 ± 0.01	-115.28 ± 13.65	271.89 ± 32.23	295.32 ± 30.15	-22.98 ± 9.80
N6	6.18 ± 0.01	0.79 ± 0.01	-180.12 ± 15.55	479.31 ± 29.96	512.04 ± 28.57	-20.60 ± 5.62
N7	6.53 ± 0.01	0.77 ± 0.01	-63.33 ± 34.51	99.35 ± 45.50	117.82 ± 42.62	-32.52 ± 49.92
N8	6.57 ± 0.01	-0.49 ± 0.01	97.83 ± 12.51	299.19 ± 43.23	314.78 ± 41.27	18.11 ± 0.57
N9	6.82 ± 0.01	-0.20 ± 0.01	-89.11 ± 16.31	349.62 ± 43.99	360.80 ± 42.82	-14.3 ± 8.55
N10	5.48 ± 0.01	0.63 ± 0.01	-121.34 ± 9.86	521.78 ± 25.41	535.70 ± 24.85	-13.09 ± 3.29
N11	5.59 ± 0.01	0.56 ± 0.01	-96.70 ± 12.51	185.05 ± 25.79	208.79 ± 23.58	-27.59 ± 12.67
N12	5.75 ± 0.01	0.39 ± 0.01	-269.23 ± 14.79	203.25 ± 28.06	337.34 ± 20.62	-52.95 ± 10.6
N13	5.89 ± 0.01	0.43 ± 0.01	61.43 ± 15.55	401.95 ± 27.68	406.62 ± 27.46	8.69 ± 3.17
N14	5.96 ± 0.01	0.44 ± 0.01	129.31 ± 17.82	497.89 ± 27.68	514.41 ± 27.16	14.56 ± 2.30
N15	6.07 ± 0.01	0.41 ± 0.01	-48.16 ± 15.93	200.22 ± 32.23	205.93 ± 31.56	-13.52 ± 12.99
N16	5.10 ± 0.01	0.12 ± 0.01	106.56 ± 21.24	236.24 ± 31.47	259.16 ± 29.99	24.28 ± 2.90
N17	5.22 ± 0.01	0.08 ± 0.01	186.19 ± 16.31	324.60 ± 22.37	374.21 ± 21.03	29.84 ± 0.93
N18	5.69 ± 0.01	0.06 ± 0.01	-32.61 ± 17.44	580.93 ± 37.92	581.84 ± 37.87	-3.21 ± 3.87
N19	6.24 ± 0.01	0.23 ± 0.01	-98.97 ± 9.48	308.67 ± 42.85	324.15 ± 40.91	-17.78 ± 7.91
N20	6.66 ± 0.01	0.24 ± 0.01	195.67 ± 14.79	304.12 ± 32.23	361.63 ± 28.26	32.76 ± 1.60
N21	6.73 ± 0.01	0.18 ± 0.01	243.07 ± 16.68	295.78 ± 40.95	382.84 ± 33.36	39.41 ± 3.97
N22	6.80 ± 0.01	0.31 ± 0.01	-59.53 ± 10.24	286.68 ± 47.02	292.80 ± 46.08	-11.73 ± 7.83
N23	6.25 ± 0.01	-0.06 ± 0.01	-91.39 ± 20.86	306.77 ± 38.68	320.09 ± 37.55	-16.59 ± 11.18
N24	6.31 ± 0.01	0.04 ± 0.01	-73.56 ± 28.44	447.08 ± 36.40	453.09 ± 36.21	-9.34 ± 8.62
N25	6.36 ± 0.01	-0.06 ± 0.01	-38.68 ± 16.31	273.40 ± 31.85	276.12 ± 31.62	-8.05 ± 8.64
N26	6.43 ± 0.01	0.07 ± 0.01	-131.96 ± 30.34	428.50 ± 47.02	448.36 ± 45.82	-17.12 ± 10.99
N27	5.47 ± 0.01	-0.26 ± 0.01	-81.15 ± 17.06	211.21 ± 28.44	226.26 ± 27.24	-21.02 ± 13.28
N28	5.98 ± 0.01	-0.35 ± 0.01	53.09 ± 14.41	503.96 ± 29.58	506.75 ± 29.46	6.01 ± 2.55
N29	6.54 ± 0.01	-0.33 ± 0.01	74.70 ± 16.68	150.54 ± 37.54	168.05 ± 34.44	26.39 ± 1.27
N30	5.91 ± 0.01	-0.58 ± 0.01	-95.94 ± 15.93	190.74 ± 28.44	213.51 ± 26.40	-26.70 ± 14.53
N31	5.72 ± 0.01	-0.77 ± 0.01	-42.47 ± 19.34	301.46 ± 30.72	304.44 ± 30.54	-8.02 ± 8.88
N32	6.24 ± 0.01	-0.78 ± 0.01	50.43 ± 19.34	284.78 ± 30.72	289.21 ± 30.44	10.04 ± 5.49
N33	6.51 ± 0.01	-0.74 ± 0.01	117.17 ± 28.06	720.86 ± 37.54	730.32 ± 37.33	9.23 ± 3.41
N34	5.61 ± 0.01	-0.80 ± 0.01	156.61 ± 19.34	396.64 ± 40.57	426.44 ± 38.40	21.55 ± 0.84
N35	7.14 ± 0.01	-0.29 ± 0.01	-77.36 ± 22.75	289.33 ± 50.81	299.49 ± 49.44	-14.97 ± 13.65
N36	6.77 ± 0.01	0.87 ± 0.01	-21.24 ± 18.96	353.41 ± 45.5	354.05 ± 45.43	-3.44 ± 7.11
N37	6.37 ± 0.01	1.17 ± 0.01	-257.10 ± 34.13	197.18 ± 56.12	324.01 ± 43.59	-52.51 ± 22.80
N38	6.73 ± 0.01	1.22 ± 0.01	144.10 ± 22.75	319.29 ± 72.05	350.30 ± 66.34	24.29 ± 3.05
N39	6.56 ± 0.01	1.33 ± 0.01	-28.06 ± 18.58	519.88 ± 58.78	520.64 ± 58.70	-3.09 ± 4.84
N40	7.06 ± 0.01	0.25 ± 0.01	-38.68 ± 10.62	487.65 ± 37.92	489.18 ± 37.81	-4.54 ± 3.20
N41	7.27 ± 0.01	0.23 ± 0.01 0.33 ± 0.01	122.10 ± 17.06	155.09 ± 35.27	197.39 ± 29.65	38.21 ± 5.07
N42	7.32 ± 0.01	0.27 ± 0.01	-200.60 ± 51.57	477.79 ± 118.31	518.19 ± 110.9	-22.78 ± 21.01

Note. N1 represents the IRS 1W bow-shock source. The positions of N sources are given with respect to the position of Sgr A* in the 2005 epoch.

Table 4

R.A. and Decl. Velocities of the Reference Stars That Are within the Uncertainties in Agreement with T. Paumard et al. (2006)

Name	$V_{R.A.}$ (km s ⁻¹)	$V_{\text{Decl.}} $ (km s ⁻¹)
IRS 1W	-89.11 ± 16.31	349.24 ± 43.99
IRS 16C	-348.48 ± 5.31	288.19 ± 8.34
IRS 16CC	-95.56 ± 5.31	266.96 ± 14.03
IRS 16NE	84.18 ± 10.62	-283.64 ± 21.61
IRS 16NW	195.29 ± 6.83	19.30 ± 4.17

would not belong to the cluster is hampered by the fact that these may still be influenced by a more coherent motion in the disk direction. On the other hand, 28 NW-ward flying sources constitute a significant overabundance that we investigate in more detail in the following section.

6. Clustering Scenarios

In the previous section, with the support of Figures 1 and 6, we showed that the N sources can be divided into two kinematically distinct categories: more abundant NW-ward flying sources and the NE-ward flying sources consisting most likely of foreground/background sources within the nuclear stellar cluster but not belonging to a possible small cluster associated with the region. In Figures 7 and 8, we show the number of sources as a function of radial distance for NW-ward and NE-ward flying sources, respectively. In these two figures, we kept the geometrical center of the N sources as the center of each population (see Table 7). In Figure 7, we demonstrate that the spatial distribution of the NW-ward flying sources is Gaussian-like; see also the fit in Figure 16 (in the Appendix), while the spatial distribution of NE-ward flying sources is flat within uncertainties (see Figure 8). Thus, based on the flying-

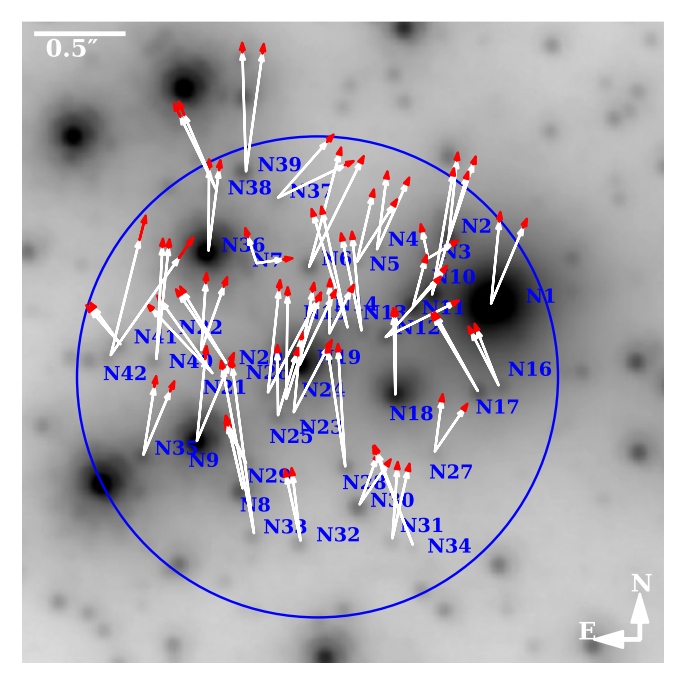


Figure 5. The K_s -band image from 2005.366 epoch with superimposed proper motions for each N source. Four arrows are shown for each source. The white arrows demonstrate the velocity vectors of each source, including the uncertainty of the velocity angle, whereas the red arrows indicate the uncertainty in the velocity magnitude. The size of the arrows is proportional to the velocity magnitude. The proper-motion vectors are based on Table 3 and the arrows are 1 order of magnitude smaller than proper motions. In total, 42 sources move northward (N sources).

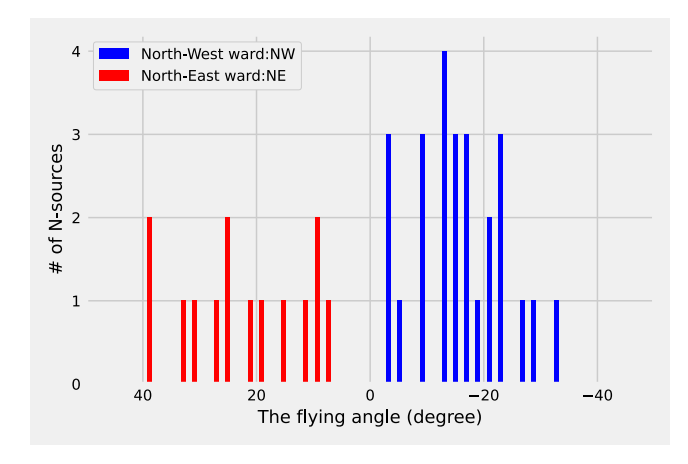


Figure 6. Distribution of flying angles of N sources. The zero angle stands for a northward flying angle. The negative angles indicate the NW-ward flying angles up to -35° , whereas the positive angles represent the NE-ward flying angles up to about 40° . There is an indication that the NW-ward sources are members of a denser association of stars, while the rest of the sources might be the foreground/background sources that are still part of the nuclear star cluster.

angle distribution as well as on the spatial distribution of the NW-ward sources, we can speculate that these sources exhibit the characteristics of a stellar cluster or an association. Therefore, we discuss two plausible scenarios that can result in a bound system or an apparent overdensity. As the first scenario, we propose the existence of an IMBH (see Section 6.1). In the second scenario, we explain the apparent overdensity on the sky as a result of an inclined disk-like distribution of stars (see Section 6.2).

The clustering hypothesis is also supported by the spatial distribution of velocities in a vector-point diagram, as shown in

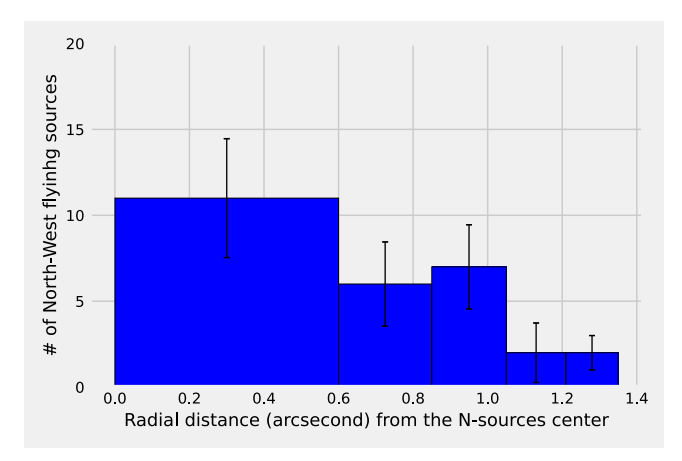


Figure 7. The spatial distribution of the NW-ward flying sources. The zero-point of the *x*-axis is at the geometrical center of the N sources. The spatial distribution is Gaussian-like.

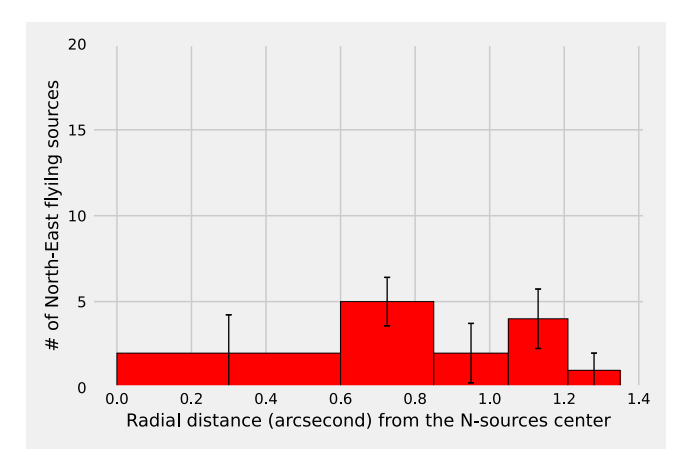


Figure 8. The spatial distribution of the NE-ward flying sources. The zero-point of the x-axis is at the geometrical center of the N sources. The spatial distribution is flat within the uncertainties.

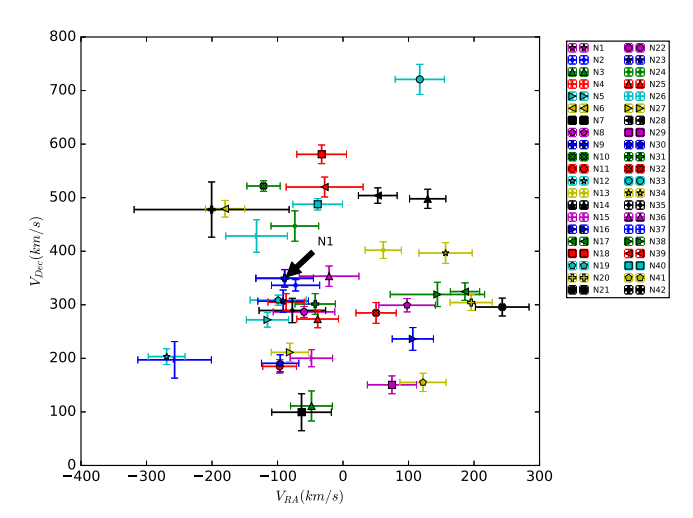


Figure 9. In this vector-point diagram we denote the spatial distribution of velocities. The position of N1/IRS 1W is depicted with a black arrow.

Figure 9. Here, the strongest clustering occurs around N1, i.e., IRS 1W, for sources moving in the NW direction (negative R. A. proper motions). The more extended distribution of sources moving predominantly NE constitutes the background source or the source in the GC stellar disk.

6.1. Putative IMBH

In the first scenario, we obtain the mass estimate of a putative IMBH for the association of NW-ward flying sources. Our comoving group of stars has a random velocity dispersion distribution. Therefore, the center of mass of the NW-ward flying association could be associated with a massive object that would prevent this group from tidal disruption. We assume that the hypothetical IMBH is located close to the geometrical center of our group of stars. In order to estimate the characteristic size of the cluster, we obtain the geometrical center of the NWward sources and consider the standard deviation of the source distribution as the characteristic radius of the cluster, which leads to the estimate of $R_c = 0.757 \pm 0.110.5$ Hence, the cluster has 10^{+3}_{-2} members within the core region. We determine the required binding mass by applying the virial theorem, $M_{\rm IMBH} \sim \sigma_{\star}^2 R_{\rm c}/G$, where $R_{\rm c} = 23 \pm 4$ mpc, G is the gravitational constant, and σ_{\star} is the stellar velocity dispersion. Hence, we assume that the NW-source cluster is relaxed, which may not be the case in general. For the calculation of the virial binding mass, we consider just sources whose total on-sky proper motion is below the escape velocity at a given projected distance from Sgr A* (at $\sim 6.245 \sim 0.25$ pc, the escape velocity is \sim 370 km s⁻¹). This way, we remove eight sources (N6, N10, N18, N24, N26, N39, N40, and N42) that exceed this value, which is caused by confusion due to their faintness.

For the remaining 20 NW sources, we consider two perpendicular directions for the estimate of σ_{\star} —along the R. A. and the decl., each corrected for the corresponding mean velocity error. For $\sigma_{\rm R.A.}=58.9^{+1.5}_{-0.7}\,{\rm km~s^{-1}}$, we obtain $M_{\rm IMBH}=18.6^{+0.3}_{-0.3}\times10^3M_{\odot}$ and for $\sigma_{\rm decl.}=64.8^{+2.6}_{-1.6}\,{\rm km~s^{-1}}$, $M_{\rm IMBH}=22.5^{+0.4}_{-0.4}\times10^3M_{\odot}^{-7}$ Thus, using the virial theorem, we obtain the first estimate of the required IMBH mass of the order of $\sim\!10^4\,M_{\odot}$ to bind the NW-ward flying sources gravitationally. The second estimate comes from the tidal stability criterion of the putative NW-ward cluster. This can be formulated using the condition that the effective cluster radius is smaller or comparable to its tidal (Hill) radius as it orbits Sgr A* SMBH, hence

$$R_{\rm c} \lesssim d_{\rm NW} \left(\frac{m_{\rm NW}}{3M_{\bullet}}\right)^{1/3},$$
 (1)

where $d_{\rm NW}\gtrsim 6.0^{\circ}.05\sim 0.242$ pc is the distance of the NW-ward flying association from Sgr A*, where the lower limit is given by the projected distance. For the SMBH mass, we take $M_{\bullet}\sim 4\times 10^6\,M_{\odot}$ and the cluster radius is estimated from the dispersion of the Gaussian fit to the number density distribution, $R_{\rm c}=23\pm 4\,{\rm mpc}$ as before. From the tidal stability condition given by Equation (1), the total mass of the

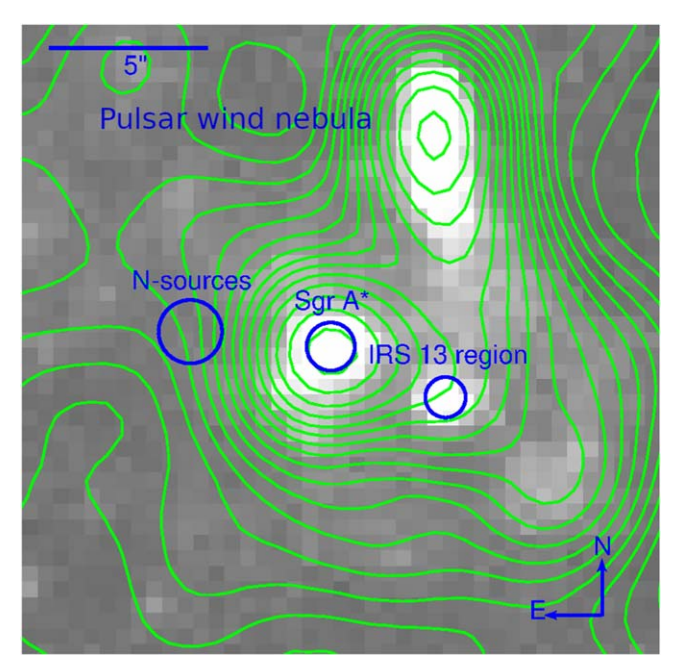


Figure 10. The Chandra X-ray image from 0.5 to 8 keV. North is up and east is to the left. Distinct X-ray bright sources are labeled, namely Sgr A^* , IRS 13, and the pulsar wind nebula. There is no significant X-ray source at the position of the N-source association. The angular scale is indicated in the upper left corner.

NW-ward cluster then is $m_{\rm NW} \gtrsim 3M_{\bullet}(R_{\rm c}/d_{\rm NW})^3$, which gives $m_{\rm NW} \gtrsim (10.3 \pm 5.4) \times 10^3 \, M_{\odot}$. Considering the total radius of the N-source region, $R_{\rm N} \sim 1.735 \sim 54$ mpc, we obtain $m_{\rm NW} \gtrsim 1.33 \times 10^5 \, M_{\odot}$. Since the stars contribute $\lesssim 10^3 \, M_{\odot}$ to the cluster mass, which follows from the total number of detected stars of the order of 10, the required mass for the tidal stability of the cluster is significantly larger and could be complemented by an IMBH of the mass $m_{\rm IMBH} \sim m_{\rm NW} \sim 10^4 - 10^5 \, M_{\odot}$, considering the total range of the N-source region size. The mass range is $\sim 10^4 - 10^5 \, M_{\odot}$ of the hypothetical IMBH associated with the NW-ward flying association, which was inferred using both the virial theorem and the tidal stability criterion, is consistent with the expected IMBH mass of $\sim 10^2 - 10^5 \, M_{\odot}$ in various stellar environments (J. E. Greene et al. 2020).

Using the 1999–2012 X-ray Chandra data available from the Chandra Search and Retrieval interface, we limit our study to the observations when Sgr A* was observed with an off-axis angle lower than 2'. This results in 84 observations with the ACIS-I or ACIS-S/HETG cameras (G. P. Garmire et al. 2003) and a total exposure time of 4.6 Ms (see details in E. Mossoux & A. Eckart 2017). The pixel scale of the Chandra X-ray data is 492 mas pixel⁻¹. In Figures 10 and 17 (in the Appendix), we plot contours at 100%, 80%, 60%, and 40% of the peak counts detected at the position of Sgr A*. In the central few arcseconds, Chandra observations have revealed both the extended X-ray emission as well as the emission from compact sources that can be associated with stars (e.g., X-ray binaries). These data confirm a thermal X-ray spectrum of IRS 13E. Fitting the spectrum with an optically thin plasma model, one finds a temperature of 2.0 keV and an unabsorbed 2–10 keV luminosity of about ${\sim}2.0\times10^{33}\,\rm erg\,s^{-1}$ for the IRS 13 region (Q. D. Wang et al. 2006; Z. Zhu et al. 2020).

No X-ray source could be identified at the position of N sources. We find that in a 1.75 diameter aperture, the X-ray

⁵ In order to fit the distribution in Figure 7 using the Gaussian function, we indicate each bin by means of three data points, at the start, center, and end of it, see Figure 16. Each data point indicates the value and the associated uncertainty of the corresponding bin. Fitting a Gaussian model on the aforementioned distribution yields the σ and its uncertainty, which we adopt as the size of the cluster and its uncertainty.

⁶ Eight sources located in the area with a radius of 18 mpc: N6, 12, 15, 19, 23, 24, 25, 26. Ten sources located in the area with the radius of 22 mpc: N5, 6, 7, 12, 15, 19, 23, 24, 25, 26. Thirteen sources located in the area with the radius of 25 mpc: N5, 6, 7, 11, 12, 15, 18, 19, 22, 23, 24, 25, 26.

⁷ These velocity dispersion values are changed by a few kilometers per second ($\sigma_{\rm R.A.}=62.3^{+1.6}_{-0.9}~{\rm km~s^{-1}}$, $\sigma_{\rm decl.}=63.9^{+1.9}_{-0.9}~{\rm km~s^{-1}}$) by removing two potential late-type stars N9 and N30, which does not impact the IMBH virial mass estimate significantly.

luminosity at the position of N sources is about three times fainter than that of IRS 13 in the 0.5–8 keV image and about 10 times fainter in the 4–8 keV image. Hence, the X-ray luminosity that can be associated with the N-source region is below $L_{\rm X} \lesssim 0.2 \times 10^{33}\,{\rm erg\,s^{-1}}$. In comparison to IRS 13E, this may indicate either a lack of hot optically thin plasma or an increased extinction from the foreground material, possibly associated with the CND (see E. Mossoux & A. Eckart 2017). In fact, L. Moser et al. (2017) report high-velocity SiO gas southwest of IRS 1W, see their Figure 11.

However, the NIR extinction maps (R. Schödel et al. 2010; A. Ciurlo et al. 2016; T. K. Fritz et al. 2016) do not support an excessively higher extinction toward that region on the arcsecond scale. On the other hand, it is unclear how the N sources in the field are located with respect to the northern arm in comparison to what Figure 8 of M. S. Nitschai et al. (2020) indicates. Therefore, a dearth of hot, optically thin plasma is also not a clear-cut explanation. Hence, to explain the lack of X-ray emission toward the N sources we are left with either a combination of the above two effects and/or an intrinsically weak X-ray emission from that region as such.

The lack of X-ray emission does not support the presence of a hypothetical IMBH accreting in a radiatively efficient way (see, e.g., R. Schödel et al. 2005). In other words, the Eddington ratio of the system $\lambda_{\rm Edd} = \kappa_{\rm bol} L_{\rm X}/L_{\rm Edd} \lesssim 3.4 \times 10^{-6} \left(\frac{L_{\rm X}}{2 \times 10^{32}\,{\rm erg\,s^{-1}}}\right)^{-1}$, where we used the bolometric correction $\kappa_{\rm bol} = 13 \left(\frac{L_{\rm X}}{10^{41}\,{\rm erg\,s^{-1}}}\right)^{-0.37}$ according to R. S. Nemmen et al. (2014), would imply a radiatively inefficient mode of accretion in the form of, e.g., advection-dominated accretion flow (ADAF), which is expected for IMBHs across various galactic environments (see, e.g., F. Pacucci & A. Loeb 2022; B. S. Seepaul et al. 2022). Under the approximation of the spherical, Bondi-like accretion of the surrounding hot plasma onto the IMBH, we can estimate the Bondi rate as

$$\dot{M}_{\rm B} = \frac{4\pi G^2 m_{\rm IMBH}^2 \mu n_{\rm a} m_{\rm H}}{c_{\rm s}^3},\tag{2}$$

where $n_{\rm a}$ is the ambient medium number density, $c_{\rm s}$ is the sound speed in the ambient plasma, $m_{\rm H}$ is the hydrogen atom mass, and μ is the mean molecular weight ($\mu \sim 0.5$ for fully ionized plasma). As an approximation, we first consider the ambient plasma properties similar to those inferred for the Bondi radius, i.e., $n_{\rm a} \sim 26~{\rm cm}^{-3}$ and $kT_{\rm a} \sim 1.3~{\rm keV}$ (F. K. Baganoff et al. 2003). For $m_{\rm IMBH} = 10^4~M_{\odot}$, we obtain $\dot{M}_{\rm B} \sim 6.2 \times 10^{-11}~M_{\odot}~{\rm yr}^{-1}$ according to Equation (2). Using the relation for the bolometric luminosity, $L_{\rm bol} = \kappa_{\rm bol} L_{\rm X} \sim 4.3 \times 10^{36} (L_{\rm X}/2 \times 10^{32}~{\rm erg~s}^{-1})^{0.63}$ and assuming the radiative efficiency of $\eta_{\rm R} \sim 0.1$, the actual X-ray luminosity is at most $L_{\rm X} \lesssim 3.8 \times 10^{30}~{\rm erg~s}^{-1}$ since the constraints on the density and the radiative efficiency are the upper limits. Hence, Bondi-like hot flow feeding the putative IMBH can explain its low X-ray emission and thus the difficulty to detect it directly within the nuclear star cluster, not only in the IRS 1W NW-ward flying region, but also in IRS 13E.

In the more precise accretion model, we attempt to construct the SED of the hot ADAF surrounding the putative IMBH of $m_{\rm IMBH} \sim 10^4 \, M_{\odot}$. The basic input parameters of the ADAF

SED are the IMBH mass m_{IMBH} and its relative accretion rate $\dot{m} \equiv \dot{M}_{\rm acc}/\dot{M}_{\rm Edd}$ (D. W. Pesce et al. 2021), where $\dot{M}_{\rm acc}$ is the actual accretion rate of the IMBH at the inner radius, which is a fraction of the Bondi accretion rate $\dot{M}_{\rm B}$, and $\dot{M}_{\rm Edd} = L_{\rm Edd}/(\eta_{\rm R} c^2)$ is Eddington accretion rate. Since for the adopted $m_{\rm IMBH} = 10^4 M_{\odot}$ we can estimate $\dot{M}_{\rm Edd}$ in a straightforward way, we need to better estimate $\dot{M}_{\rm acc}$ from $\dot{M}_{\rm B}$, see Equation (2). The sound speed of the flow can be estimated from the virial theorem, assuming that the gas and the stellar motion are virialized. Then, we can associate the mean quadratic velocity of the gas $\langle v^2 \rangle$ with the stellar velocity dispersion, $\langle v^2 \rangle = \sigma_{\star}^2 = 3\sigma_1^2$, where σ_1 is a one-dimensional dispersion along any direction. The average one-dimensional dispersion from R.A. and decl. dispersions is $\sigma_i \sim 62 \,\mathrm{km \, s^{-1}}$. Then, we can estimate the sound speed in the gas as $c_s = \langle v^2 \rangle^{1/2} / \sqrt{3} \sim \sigma_i \sim 62 \text{ km s}^{-1}$, which corresponds to the temperature of $T_a \sim 2.3 \times 10^5$ K or ~ 19.9 eV. The inferred sound speed of the gas being captured by the IMBH then yields the estimate of the capture or the Bondi radius:

$$R_{\rm B} = \frac{2Gm_{\rm IMBH}}{c_{\rm s}^2}$$

$$= 22.5 \left(\frac{m_{\rm IMBH}}{10^4 \, M_{\odot}}\right) \left(\frac{T_{\rm a}}{2.3 \times 10^5 \, \rm K}\right)^{-1} \rm mpc \sim 0.756, \quad (3)$$

which is comparable to the cluster core radius R_c .

For the estimate of the actual accretion rate $\dot{M}_{\rm acc}$, we use the power-law relation between the accretion rate at the Bondi radius $R_{\rm B}$ and the inner radius, which we set to $R_{\rm in}=100\,Gm_{\rm IMBH}/c^2$ following B. S. Seepaul et al. (2022, and references therein):

$$\dot{M}_{\rm acc} = \dot{M}_{\rm B} \left(\frac{R_{\rm in}}{R_{\rm B}}\right)^p,\tag{4}$$

where the power-law index is set to p = 0.5. To estimate the mean density of the ambient flow n_a , we assume a setup where N_{\star} stars are uniformly distributed in the sphere of radius R_c , which represents the cluster core radius. Then, the mean number density can be inferred from the stationary wind outflow at the mean distance between the star and the IMBH or

$$n_{\rm a} = \frac{N_{\star} \dot{m}_{\rm w}}{4\pi \bar{r}^2 \mu m_{\rm H} v_{\rm w}} = \left(\frac{3N_{\star}}{4\pi}\right)^{5/3} \frac{\dot{m}_{\rm w}}{v_{\rm w}} (3\mu m_{\rm H} R_{\rm c}^2)^{-1},\tag{5}$$

where $\dot{m}_{\rm w}$ is the mean mass-loss rate per star and $v_{\rm w}$ is the terminal stellar-wind velocity. Combining Equations (2), (4), and (5), along with the inferred sound speed, we obtain the Eddington ratio of the IMBH of $\dot{m} = \dot{M}_{\rm acc} / \dot{M}_{\rm Edd} \sim 1.7 \times 10^{-5}$ for the upper limit of the stellar mass-loss rate $(\dot{m}_{\rm w} = 10^{-5} \, M_{\odot} \, {\rm yr}^{-1}, \ v_{\rm w} = 10^3 \, {\rm km \, s}^{-1}) \ {\rm and} \ \dot{m} = 1.7 \times 10^{-8}$ for a lower stellar mass-loss rate of $\dot{m}_{\rm w} = 10^{-8} \, M_{\odot} \, {\rm yr}^{-1}$ $(v_{\rm w} = 10^3 \, {\rm km \, s}^{-1})$. This range of relative accretion rates of the putative IMBH at the core of the NW cluster can be used to calculate the SED of the corresponding ADAF (D. W. Pesce et al. 2021) and hence the observability of the candidate IMBH across different wavelengths. In Figure 11, we show ADAF SEDs that were calculated using the code LLAGNSED (D. W. Pesce et al. 2021) for different accretion rates (see the legend). For decreasing accretion rates, SED peaks shift toward longer wavelengths from the infrared toward the radio/

 $^{^{\}overline{8}}$ The Eddington luminosity is estimated using the standard upper limit for the steady spherical accretion, $\dot{L}_{\rm Edd} = 4\pi G m_{\rm IMBH} m_{\rm p} c/\sigma_{\rm T}$.

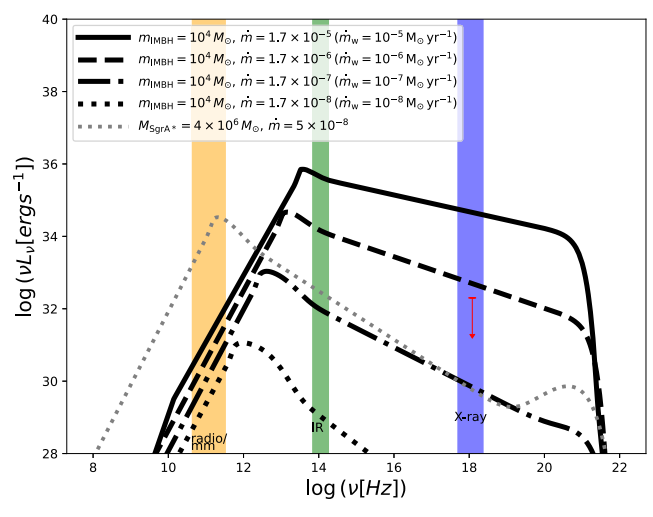


Figure 11. SEDs of ADAFs associated with the putative IMBH at the geometrical center of the NW-ward flying sources. Different black lines stand for the accretion rates according to the legend. For comparison, we also show the SED of Sgr A^* (gray dotted line). The red point depicts the X-ray emission upper limit.

millimeter domain. For comparison, we also depict the SED of Sgr A*, which peaks in the millimeter domain. Using the X-ray upper limit of $\leq 0.2 \times 10^{33} \, \mathrm{erg \, s^{-1}}$, we can constrain the Eddington ratio to $\dot{m} < 1.7 \times 10^{-6}$, for which the feeding by $N_{\star} = 10$ stars with $\dot{m}_{\mathrm{w}} \lesssim 10^{-6} \, M_{\odot} \, \mathrm{yr^{-1}}$ within the cluster core is sufficient.

In case there is no IMBH at the center of the NW-ward flying association, it will be tidally disrupted on the orbital timescale,

$$P_{\text{orb}} \gtrsim 2\pi \frac{d_{\text{NW}}^{3/2}}{\sqrt{GM_{\bullet}}}$$

$$\sim 5577 \left(\frac{d_{\text{NW}}}{0.242 \text{ pc}}\right)^{3/2} \left(\frac{M_{\bullet}}{4 \times 10^6 M_{\odot}}\right)^{-1/2} \text{yr}, \qquad (6)$$

which is such a short timescale in comparison with the stellar lifetime that it is unlikely that we observe the NW-ward group just at the beginning of tidal dissociation. Therefore, it is more likely that either the group is bound by a quiescent IMBH or the overdensity is due to the projection effect, in particular, the inclined disk-like distribution of stars that we discuss in the following subsection.

Eventually, the lifetime of the IMBH-bound stellar association similar to the NW-ward flying group is given by the dynamical friction timescale, during which the IMBH inspirals toward Sgr A*,

$$\tau_{\rm df} = \frac{3}{8} \sqrt{\frac{2}{\pi}} \frac{\sigma_{\star}^{3}}{G^{2} \rho_{\star} m_{\rm IMBH} \ln \Lambda}$$

$$\sim 3 \times 10^{5} \left(\frac{\sigma_{\star}}{88 \text{ km s}^{-1}}\right)^{3} \left(\frac{\rho_{\star}}{2.4 \times 10^{5} M_{\odot} \text{ pc}^{-3}}\right)^{-1}$$

$$\times \left(\frac{m_{\rm IMBH}}{10^{4} M_{\odot}}\right)^{-1} \left(\frac{\ln \Lambda}{15}\right)^{-1} \text{ yr,}$$
(7)

where σ_{\star} is the stellar velocity dispersion that we scale to $\sigma_{\star} \sim 88 \, \mathrm{km \, s^{-1}}$ according to the $M_{\bullet} - \sigma_{\star}$ relation (K. Gültekin et al. 2009); the stellar mass density ρ_{\star} is estimated using the condition that there is the stellar mass of $M_{\star}(r < r_{\mathrm{h}}) \sim 2 \, M_{\bullet}$

inside the Sgr A* sphere of influence, which is $r_{\rm h} \sim 2\,{\rm pc}$ (D. Merritt 2013); the IMBH mass is scaled to $m_{\rm IMBH} \sim 10^4\,M_\odot$ following the previous estimates, and the Coulomb logarithm is estimated as $\ln\Lambda \sim \ln(M_\bullet/M_\odot) \sim 15$. Hence, the stellar association would be disrupted on the timescale of the order of $\tau_{\rm df}$ as the IMBH inspirals via dynamical scattering through the nuclear star cluster. The tidal stripping of the stellar cluster during the IMBH inspiral toward the SMBH may be one of the mechanisms of how early-type stars of spectral types O and B are deposited close to the SMBH on the scale of $\sim 0.01\,{\rm pc}$.

6.2. Disk-like Distribution Projection

T. Paumard et al. (2006) and J. R. Lu et al. (2009) categorized IRS 1W as a member of the CW disk and IRS 13E members were introduced as members of the CCW disk. However, later S. Yelda et al. (2014) did not find evidence for the existence of the CCW disk and J. Sanchez-Bermudez et al. (2014) also did not categorize IRS 1W as a member of the CW disk based on the bow-shock orientation and the proper motion. The fact that the N sources and the IRS 13 region are located on opposite sides to each other at similar distances from Sgr A* (6" and 4", respectively), suggests that their appearance may in fact be the result of the projection of a disk-like distribution, such as the CW disk of young He-stars and/or dust-enshrouded stars.

Looking at the proper-motion velocities of individual sources under the assumption of the disk scenario, one has to bear in mind that this is not a very stringent picture. We are not dealing with a thin disk with orbiting stars fixed to it. Rather, the disk has a nonvanishing thickness, i.e., there is a certain velocity dispersion in the direction perpendicular to the disk plane. In addition, the disk stars are on individual orbits with varying orbital elements (i.e., the orbit orientation and eccentricity). Hence, the current data does not allow us to make firm statements on their disk-deprojected motion.

We show that the corresponding projected stellar surface density on the sky may be about a factor of 2 higher than the density of the northern and southern projected disk sections. We can estimate this effect in the following way. We assume that the disk-forming fraction of stars is arranged in a disk with an inclination of $i = 10^{\circ}$ (Y. Levin & A. M. Beloborodov 2003; J. R. Lu et al. 2008), with an outer radius of $r_{\text{out}} = 5''$, and an inner radius of $r_{\text{in}} = 1.''.5$ (shown in Figure 12). We can then calculate cross sections through that disk system as

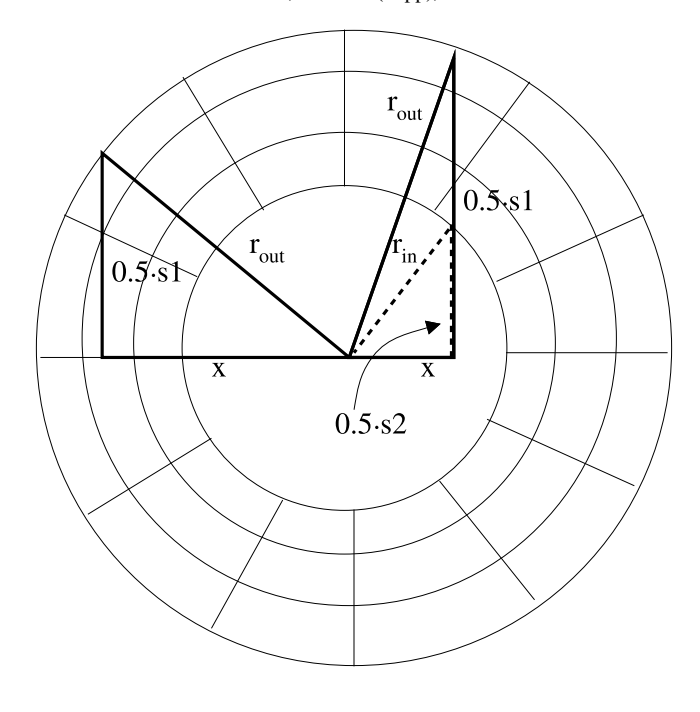
$$s_1 = 2\sqrt{|r_{\text{out}}^2 - x^2|}$$
 (8)

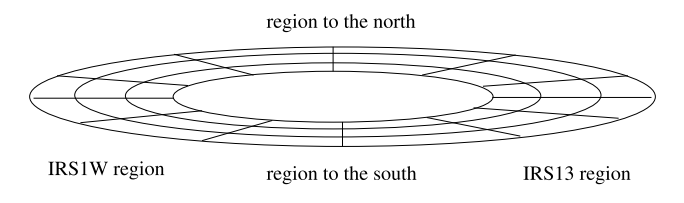
(see the left side of the upper panel in Figure 12),

$$s_2 = s_1 - 2\sqrt{|r_{\rm in}^2 - x^2|} \tag{9}$$

(see the right side of the upper panel in Figure 12).

The projected surface density ρ is proportional to $s_1/\cos(i)$ for the regions beyond the inner radius $r_{\rm in}$ and is proportional to $\frac{1}{2}s_2/\cos(i)$ for the regions within the inner radius $r_{\rm in}$ to the north and the south of Sgr A*. The fact that both N sources and IRS 13 lie on the opposite sides of Sgr A* at a rather similar distance may support this model. Hence, the overdensity of these compact stellar systems could be explained by the projection effect in which the excess in velocity dispersion is given to a large part by the disk dynamics, see Figure 13.





inclination 80 degrees

Figure 12. Top: face-on view of the east-west (EW) stellar disk system with outer and inner radii given in the text. For the case of s1, we indicated the corresponding quantities. Bottom: the disk system is inclined by 80° . The clustering at the eastern and western tips of the disk becomes evident.

7. Conclusions

For the first time, we show that N sources are northward-moving sources located in the Galactic center in the vicinity of the bow-shock source IRS 1W. We demonstrate that these sources possess a Gaussian-like number density distribution with respect to the geometrical center. The overdensity is apparent in comparison with the number of sources in random test regions at a comparable distance from Sgr A*. These circular regions have the same length scale as the N-source region. The mean number of the detected sources in our eleven test regions is 14.6 ± 1.5 , while the number of N sources is 42, which indicates that the N-source group is potentially a stellar association in the vicinity of Sgr A*.

Further investigation of the proper motions of N sources reveals that N sources can be divided into two categories. One category encompasses the NW-ward flying sources, which show a spatial Gaussian number density distribution, while the NE-ward flying sources have a rather spatially flat distribution. Therefore, the NW-ward flying sources could potentially be bound or have a common origin, while NE-ward flying sources most likely consist of local background/foreground stars that are part of the nuclear star cluster.

The high concentration of the N sources, mainly the NW-ward flying group, can be interpreted in terms of the stellar

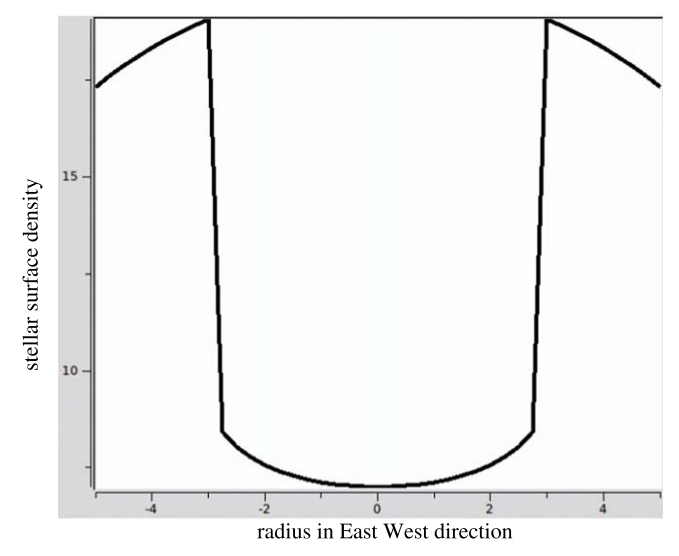


Figure 13. Stellar sky surface density in arbitrary units as a function of radius in the EW direction in arcseconds. Here also, the clustering at the eastern and western tips of the disk becomes evident. The source density is almost a factor of 2 higher than in the northern and southern parts of the disk.

cluster that is kept stable by the central IMBH or it could be the result of a disk-like stellar distribution that is projected at a high angle.

The first scenario is supported by a likely occurrence of IMBHs in the Galactic center. One possible formation channel is a series of collisions of stellar mass black holes with main-sequence stars, which was analyzed by S. C. Rose et al. (2022). This mechanism appears quite efficient and it can produce IMBHs of mass $\lesssim 10^4 \, M_{\odot}$, which is within the current uncertainties of the IMBH mass constraints for IRS 1W association, specifically using either the velocity dispersion of NW-ward flying sources or the tidal stability criterion.

Another potential way is the cluster infall scenario from larger scales (see, e.g., G. Fragione 2022, and references therein), which assumes that massive clusters, such as young star-forming clusters or globular clusters host IMBHs with a certain occupation fraction. In this regard, the NW-ward flying group could be a remnant, tidally stable core of such an infalling massive cluster. Using the Chandra X-ray telescope data, we show that such an IMBH would have a low Eddington ratio of $\dot{m} < 1.7 \times 10^{-6}$, hence would be surrounded by an X-ray faint advection-dominated flow. Future spectroscopic data collected by the James Webb Space Telescope and 30/40 m class telescopes will be crucial for a better understanding of the stellar composition of the N sources, and this may also help to clarify their potential origin in a common cluster whose core can only be kept stable by an IMBH at a given distance from Sgr A*. On the other hand, the short dynamical friction timescale of an IMBH within the nuclear stellar cluster (NSC) of the order of 10⁵ yr, see Equation (7), implies that the IMBH, including its stellar system, is a dynamically transient phenomenon in the dense environment of the NSC, which also applies to the IRS 13 association.

The second scenario is supported by an exceptional distribution of cluster-like stellar associations in the vicinity of Sgr A*. Specifically, the IRS 13 and the N-source areas are positioned at \sim 4" southwest and \sim 6" northeast of Sgr A*, respectively, nearly along the same line, which raises the possibility that the observed overdensities may actually be

formed due to the projection when the two regions are situated on the same stellar disk with the characteristics similar to that of the CW stellar disk.

In the current investigation, we do not find a strong preference for any of the two models. It is therefore necessary to conduct detailed spectroscopic measurements to rule out one of the models. More information about the orbital properties of these sources, in particular spectroscopically determined line-of-sight velocities, will be crucial for the further study of this and similar regions.

Acknowledgments

We thank an anonymous referee for constructive comments that helped to improve the manuscript. This work was supported in part by SFB 956, "Conditions and Impact of Star Formation." S.E.H. is a member of the International Max Planck Research School for Astronomy and Astrophysics at the Universities of Bonn and Cologne. We thank the Collaborative Research Centre 956, subproject A02, funded by the Deutsche Forschungsgemeinschaft (DFG)—project ID 184018867. M.Z. acknowledges the financial support by the GAČR Junior Star

No. GM24-10599M, "Stars in galactic nuclei: interrelation with massive black holes." V.K. acknowledges the Czech Science Foundation grant No. 21-06825X and the Czech Ministry of Education, Youth and Sports Research Infrastructure grant No. LM2023047.

Appendix

Here, we include additional plots and tables relevant for the study of the stellar association around IRS 1W. In Figure 14, we depict 11 regions chosen randomly to compare the number of stars inside them with the region around IRS 1W (N-source region). The proper motion of the N2 star is shown in Figure 15. In Figure 16, we show a 4–8 keV Chandra X-ray image of the Galactic center's central parsec including the N-source region. In Figure 17, we illustrate that the NW-moving sources have a Gaussian-like distribution, which is demonstrated by a Gaussian fit. Near-infrared magnitudes of the N sources are listed in Table 5, while the color indices are summarized in Table 6. Table 7 lists the detemined geometrical centers of the N sources, NW-, and NE-moving groups.

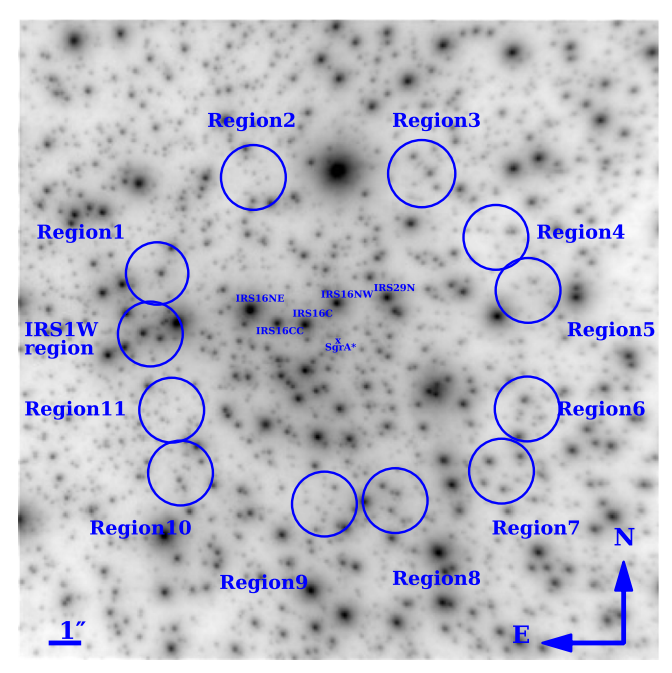


Figure 14. The K_s -band from 2005.366 observation. The K_s -band image denotes 11 regions in addition to the assumed region of IRS 1W. These 11 regions are chosen randomly in order to identify the number of sources in each one. The only criterion is the distance from Sgr A*; all regions are located at a distance of almost 6" from Sgr A*. The radii of all circular regions are about 1."3.

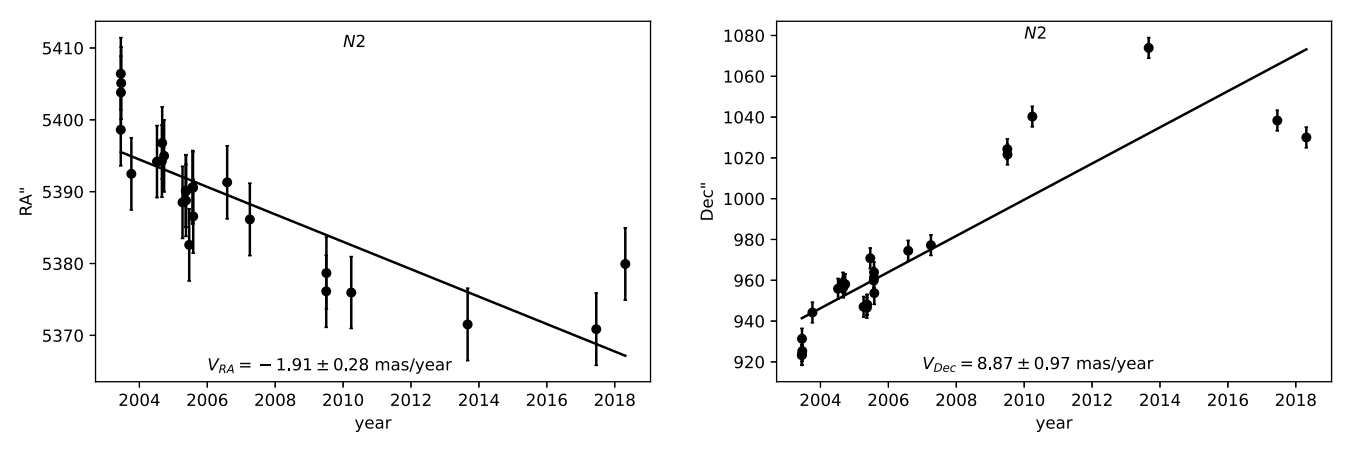


Figure 15. The plots show the derived positions of the N2 star as a function of time, along with the best-fitting proper motions. The left panel is along the R.A. and the right panel is along the decl. The slope of each best-fitting line is given in Table 3 (in kilometers per second).

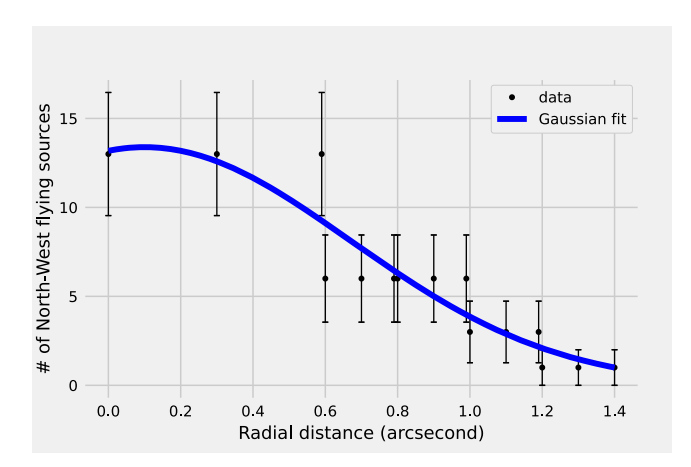


Figure 16. Gaussian fit of the spatial distribution of NW-flying sources.

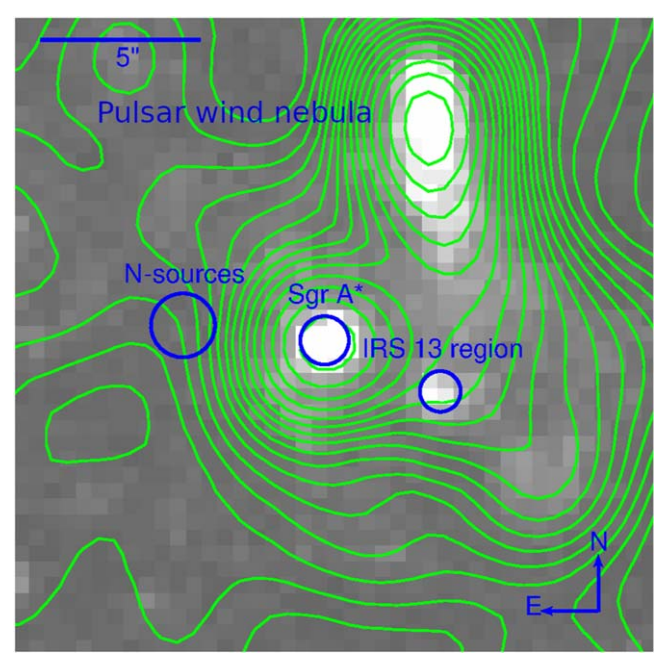


Figure 17. The Chandra X-ray image from 4 to 8 keV. The north is up and east is to the left. Distinct X-ray bright sources are labeled, namely Sgr A*, IRS 13, and the pulsar wind nebula. There is no significant X-ray source at the position of the N-source association. The angular scale is indicated in the upper left corner.

Table 5Magnitudes of Sources

Name	Н	K	L	Name	$H-K_s$	$K_s - L'$
N1	12.05 ± 0.03	9.18 ± 0.02	6.19 ± 0.05	N1	2.867 ± 0.375	2.984 ± 0.552
N2	14.62 ± 0.79	12.26 ± 0.29	10.45 ± 0.10	N2	2.366 ± 0.304	1.805 ± 0.84
N3	15.03 ± 0.03	13.43 ± 0.32	10.46 ± 0.21	N3	1.604 ± 0.386	2.964 ± 0.323
N4	16.03 ± 0.38	14.57 ± 0.61	11.73 ± 0.32	N4	1.467 ± 0.686	2.839 ± 0.712
N5	17.10 ± 1.17	14.71 ± 0.33	11.98 ± 0.35	N5	2.392 ± 0.481	2.737 ± 1.216
N6	15.73 ± 0.45	13.32 ± 0.03	11.65 ± 0.18	N6	2.406 ± 0.177	1.674 ± 0.452
N7	15.50 ± 0.16	15.01 ± 0.85	12.77 ± 0.44	N7	0.491 ± 0.957	2.233 ± 0.865
N8	15.28 ± 0.55	12.79 ± 0.22	11.21 ± 0.19	N8	2.486 ± 0.295	1.582 ± 0.592
N9	12.81 ± 0.03	9.94 ± 0.07	9.06 ± 0.02	N9	2.875 ± 0.069	0.877 ± 0.074
N10	13.41 ± 0.18	11.27 ± 0.04	10.19 ± 1.15	N10	2.146 ± 1.156	1.073 ± 0.183
N11	14.17 ± 0.49	11.64 ± 0.15	10.57 ± 1.01	N11	2.537 ± 1.021	1.066 ± 0.514
N12	15.79 ± 0.04	13.21 ± 0.03	10.36 ± 0.37	N12	2.575 ± 0.371	2.850 ± 0.050
N13	16.38 ± 1.61	13.90 ± 0.43	10.68 ± 0.25	N13	2.478 ± 0.500	3.226 ± 1.665
N14	15.33 ± 0.31	14.22 ± 1.45	10.46 ± 0.22	N14	1.107 ± 1.465	3.763 ± 1.480
N15	14.73 ± 0.32	12.94 ± 0.26	10.10 ± 0.24	N15	1.791 ± 0.354	2.836 ± 0.409
N16	15.41 ± 0.18	13.55 ± 0.68	10.29 ± 0.29	N16	1.865 ± 0.736	3.253 ± 0.702
N17	15.43 ± 1.35	13.07 ± 0.97	10.28 ± 0.30	N17	2.362 ± 1.014	2.782 ± 1.659
N18	13.47 ± 0.15	10.98 ± 0.21	8.55 ± 0.21	N18	2.482 ± 0.295	2.431 ± 0.255
N19	12.44 ± 0.05	10.07 ± 0.13	9.08 ± 0.13	N19	2.369 ± 0.182	0.983 ± 0.138
N20	17.01 ± 0.53	14.24 ± 0.17	13.49 ± 0.79	N20	2.775 ± 0.805	0.751 ± 0.556
N21	17.04 ± 0.69	15.21 ± 1.54	12.87 ± 0.44	N21	1.829 ± 1.604	2.333 ± 1.689
N22	18.36 ± 0.65	14.96 ± 0.63	13.44 ± 0.76	N22	3.406 ± 0.992	1.518 ± 0.909
N23	16.01 ± 0.81	14.18 ± 0.52	11.60 ± 0.28	N23	1.832 ± 0.592	2.588 ± 0.964
N24	15.12 ± 0.48	14.90 ± 0.27	11.24 ± 0.28	N24	0.219 ± 0.393	3.660 ± 0.552
N25	15.97 ± 0.54	13.72 ± 0.29	11.89 ± 0.11	N25	2.246 ± 0.315	1.828 ± 0.613
N26	15.64 ± 0.15	14.29 ± 0.75	11.62 ± 0.19	N26	1.348 ± 0.773	2.669 ± 0.763
N27	16.78 ± 0.22	14.89 ± 0.26	11.79 ± 0.38	N27	1.892 ± 0.459	3.099 ± 0.343
N28	16.85 ± 1.02	14.12 ± 0.31	12.47 ± 0.22	N28	2.723 ± 0.386	1.652 ± 1.071
N29	16.19 ± 1.35	14.36 ± 1.79	12.47 ± 0.22	N29	1.833 ± 1.802	1.885 ± 2.242
N30	16.01 ± 0.11	13.53 ± 0.08	12.26 ± 0.30	N30	2.475 ± 0.305	1.268 ± 0.130
N31	18.33 ± 1.95	15.52 ± 0.15	13.23 ± 0.28	N31	2.807 ± 0.317	2.291 ± 1.953
N32	17.46 ± 0.35	14.82 ± 0.12	13.35 ± 0.13	N32	2.638 ± 0.180	1.478 ± 0.373
N33	16.64 ± 0.36	14.80 ± 0.09	12.86 ± 0.29	N33	1.839 ± 0.303	1.934 ± 0.366
N34	19.22 ± 1.77	16.43 ± 0.37	13.95 ± 1.24	N34	2.795 ± 1.291	2.474 ± 1.810
N35	16.79 ± 0.08	15.19 ± 0.28	13.15 ± 0.30	N35	1.601 ± 0.450	2.041 ± 1.102
N36	12.26 ± 0.02	9.71 ± 0.01	8.93 ± 0.03	N36	2.545 ± 0.014	0.779 ± 0.022
N37	16.15 ± 0.05	15.14 ± 2.39	13.75 ± 0.20	N37	1.601 ± 0.409	2.041 ± 0.291
N38	15.78 ± 0.15	13.10 ± 0.04	12.82 ± 0.37	N38	1.008 ± 2.400	1.386 ± 2.392
N39	17.06 ± 0.72	14.61 ± 0.27	14.90 ± 0.23	N39	2.686 ± 0.375	0.275 ± 0.151
N40	16.40 ± 0.43	14.28 ± 0.33	13.55 ± 0.08	N40	2.447 ± 0.357	-0.284 ± 0.770
N41	16.71 ± 1.87	14.52 ± 0.22	13.58 ± 0.06	N41	2.118 ± 0.339	0.735 ± 0.543
N42	15.41 ± 1.01	13.02 ± 0.44	12.35 ± 0.08	N42	2.191 ± 0.232	0.94 ± 3.480
IRS 10W	12.74 ± 0.08	10.11 ± 0.06	6.99 ± 0.03	IRS 10W	2.626 ± 0.063	3.122 ± 0.096
IRS 21	14.03 ± 0.24	10.71 ± 0.00 10.72 ± 0.21	6.97 ± 0.03 6.97 ± 0.10	IRS 21	3.307 ± 0.235	3.748 ± 0.323
IRS 16NW	11.39 ± 0.05	9.26 ± 0.03	8.62 ± 0.02	IRS 16NW	2.132 ± 0.036	0.638 ± 0.057
	11.57 ± 0.05	7.20 ± 0.03	0.02 ± 0.02		2.132 ± 0.030	0.030 ± 0.037

Table 7
Geometric Centers of N Sources, NW-flying Sources, and NE-flying Sources
Calculated as Medians of the Corresponding Values in Table 3

Name	$\Delta \alpha$ (arcsec)	$\Delta \delta$ (arcsec)
Geometric center of N sources (42)	6.24 ± 0.47	0.25 ± 0.42
Geometric center of NW-flying sources (28)	6.21 ± 0.48	0.35 ± 0.42
Geometric center of NE-flying sources (14)	6.38 ± 0.38	0.10 ± 0.39

Note. The geometric center of N sources (total) is in between NW-flying and NE-flying sources. It is closer to NW-flying sources since they are twice as numerous as NE-flying sources. The uncertainty of the median value is calculated as the median of the measurement offsets from the median.

ORCID iDs

S. Elaheh Hosseini https://orcid.org/0000-0002-3004-6208

Andreas Eckart https://orcid.org/0000-0001-6049-3132

Michal Zajaček https://orcid.org/0000-0001-6450-1187

Silke Britzen https://orcid.org/0000-0001-9240-6734

Harshitha K. Bhat https://orcid.org/0000-0002-4408-0650

Vladimír Karas https://orcid.org/0000-0002-5760-0459

References

```
Ali, B., Paul, D., Eckart, A., et al. 2020, ApJ, 896, 100
Baganoff, F. K., Maeda, Y., Morris, M., et al. 2003, ApJ, 591, 891
Balick, B., & Brown, R. L. 1974, ApJ, 194, 265
Bartko, H., Martins, F., Fritz, T. K., et al. 2009, ApJ, 697, 1741
Bartko, H., Martins, F., Trippe, S., et al. 2010, ApJ, 708, 834
Becklin, E. E., & Neugebauer, G. 1975, ApJL, 200, L71
Berukoff, S. J., & Hansen, B. M. S. 2006, ApJ, 650, 901
Bhat, H. K., Sabha, N. B., Zajaček, M., et al. 2022, ApJ, 929, 178
Blum, R. D., Sellgren, K., & Depoy, D. L. 1996, ApJ, 470, 864
Cantiello, M., Jermyn, A. S., & Lin, D. N. C. 2021, ApJ, 910, 94
Ciurlo, A., Paumard, T., Rouan, D., & Clénet, Y. 2016, A&A, 594, A113
Clénet, Y., Rouan, D., Gendron, E., et al. 2004, A&A, 417, L15
Dinh, C. K., Ciurlo, A., Morris, M. R., et al. 2024, AJ, 167, 41
Diolaiti, E., Bendinelli, O., Bonaccini, D., et al. 2000, in ASP Conf. Ser. 216,
   Astronomical Data Analysis Software and Systems IX, ed. N. Manset,
   C. Veillet, & D. Crabtree (San Francisco, CA: ASP), 623
Eckart, A., & Genzel, R. 1996, Natur, 383, 415
Eckart, A., Hüttemann, A., Kiefer, C., et al. 2017, FoPh, 47, 553
Eckart, A., Moultaka, J., Viehmann, T., Straubmeier, C., & Mouawad, N. 2004,
    ApJ, 602, 760
Eckart, A., Mužić, K., Yazici, S., et al. 2013, A&A, 551, A18
E. H. T. Collaboration, Akiyama, K., Alberdi, A., et al. 2022, ApJL, 930, L12
Eisenhauer, F., Schödel, R., Genzel, R., et al. 2003, ApJL, 597, L121
Ekers, R. D., van Gorkom, J. H., Schwarz, U. J., & Goss, W. M. 1983, A&A,
   122, 143
Feldmeier-Krause, A., Neumayer, N., Schödel, R., et al. 2015, A&A, 584, A2
Fragione, G. 2022, ApJ, 939, 97
Fritz, T. K., Chatzopoulos, S., Gerhard, O., et al. 2016, ApJ, 821, 44
Fritz, T. K., Gillessen, S., Dodds-Eden, K., et al. 2010, ApJ, 721, 395
Garmire, G. P., Bautz, M. W., Ford, P. G., Nousek, J. A., & Ricker, G. R. J.
   2003, Proc. SPIE, 4851, 28
Genzel, R., Eisenhauer, F., & Gillessen, S. 2010, RvMP, 82, 3121
Genzel, R., Eisenhauer, F., & Gillessen, S. 2024, A&ARv, 32, 3
Genzel, R., Schödel, R., Ott, T., et al. 2003, ApJ, 594, 812
Gerhard, O. 2001, ApJL, 546, L39
Ghez, A. M., Duchêne, G., Matthews, K., et al. 2003, ApJL, 586, L127
Ghez, A. M., Klein, B. L., Morris, M., & Becklin, E. E. 1998, ApJ, 509, 678
Goss, W. M., & McGee, R. X. 1996, in ASP Conf. Ser. 102, The Galactic
   Center, ed. R. Gredel (San Francisco, CA: ASP), 369
GRAVITY Collaboration, Abuter, R., Accardo, M., et al. 2019a, Msngr,
   178, 26
GRAVITY Collaboration, Abuter, R., Amorim, A., et al. 2019b, A&A,
   625, L10
```

```
Greene, J. E., Strader, J., & Ho, L. C. 2020, ARA&A, 58, 257
Gültekin, K., Richstone, D. O., Gebhardt, K., et al. 2009, ApJ, 698, 198
Hansen, B. M. S., & Milosavljević, M. 2003, ApJL, 593, L77
Hobbs, A., & Nayakshin, S. 2009, MNRAS, 394, 191
Jalali, B., Pelupessy, F. I., Eckart, A., et al. 2014, MNRAS, 444, 1205
Kunneriath, D., Eckart, A., Vogel, S. N., et al. 2012, A&A, 538, A127
Lebofsky, M. J., Rieke, G. H., & Tokunaga, A. T. 1982, ApJ, 263, 736
Levin, Y., & Beloborodov, A. M. 2003, ApJ, 590, L33
Lo, K. Y., & Claussen, M. J. 1983, Natur, 306, 647
Lu, J. R., Ghez, A. M., Hornstein, S. D., et al. 2008, ApJ, 690, 1463
Lu, J. R., Ghez, A. M., Hornstein, S. D., et al. 2009, ApJ, 690, 1463
Maillard, J. P., Paumard, T., Stolovy, S. R., & Rigaut, F. 2004, A&A, 423, 155
Mapelli, M., & Gualandris, A. 2016, LNP, 905, 205
McMillan, S. L. W., & Portegies Zwart, S. F. 2003, ApJ, 596, 314
Merritt, D. 2013, Dynamics and Evolution of Galactic Nuclei (Princeton, NJ:
  Princeton Univ. Press)
Morris, M. 1992, in AIP Conf. Proc. 278, Back to the Galaxy, ed. S. S. Holt &
  F. Verter (Melville, NY: AIP), 21
Morris, M. 1993, ApJ, 408, 496
Moser, L., Sánchez-Monge, Á., Eckart, A., et al. 2017, A&A, 603, A68
Mossoux, E., & Eckart, A. 2017, MNRAS, 474, 3787
Moultaka, J., Eckart, A., Schödel, R., Viehmann, T., & Najarro, F. 2005, A&A,
  443, 163
Mužić, K., Eckart, A., Schödel, R., Meyer, L., & Zensus, A. 2007, A&A,
  469, 993
Mužić, K., Schödel, R., Eckart, A., Meyer, L., & Zensus, A. 2008, A&A,
  482, 173
Nayakshin, S., Dehnen, W., Cuadra, J., & Genzel, R. 2006, MNRAS,
  366, 1410
Nemmen, R. S., Storchi-Bergmann, T., & Eracleous, M. 2014, MNRAS,
  438, 2804
Nitschai, M. S., Neumayer, N., & Feldmeier-Krause, A. 2020, ApJ, 896, 68
Ott, T., Eckart, A., & Genzel, R. 1999, in ASP Conf. Ser. 186, The Central
   Parsecs of the Galaxy, ed. H. Falcke et al. (San Francisco, CA: ASP), 310
Pacucci, F., & Loeb, A. 2022, ApJL, 940, L33
Paumard, T., Genzel, R., Martins, F., et al. 2006, ApJ, 643, 1011
Peißker, F., Zajaček, M., Eckart, A., et al. 2021, ApJ, 923, 69
Peißker, F., Zajaček, M., Labaj, M., et al. 2024, ApJ, 970, 74
Peißker, F., Zajaček, M., Thomkins, L., et al. 2023, ApJ, 956, 70
Pesce, D. W., Palumbo, D. C. M., Narayan, R., et al. 2021, ApJ, 923, 260
Portegies Zwart, S. F., Baumgardt, H., McMillan, S. L. W., et al. 2006, ApJ,
  641, 319
Portegies Zwart, S. F., & McMillan, S. L. W. 2002, ApJ, 576, 899
Rasio, F. A., Freitag, M., & Gürkan, M. A. 2004, Carnegie Observatories
  Centennial Symp. Coevolution of Black Holes and Galaxies, ed. L. C. Ho
  (Cambridge: Cambridge Univ. Press), 138
Reid, M. J. 1993, ARA&A, 31, 345
Rizzuto, F. P., Naab, T., Spurzem, R., et al. 2021, MNRAS, 501, 5257
Rose, S. C., Naoz, S., Sari, R., & Linial, I. 2022, ApJL, 929, L22
Sanchez-Bermudez, J., Schödel, R., Alberdi, A., et al. 2014, A&A, 567, A21
Schödel, R., Eckart, A., Iserlohe, C., Genzel, R., & Ott, T. 2005, ApJL,
Schödel, R., Merritt, D., & Eckart, A. 2009, A&A, 502, 91
Schödel, R., Najarro, F., Muzic, K., & Eckart, A. 2010, A&A, 511, A18
Seepaul, B. S., Pacucci, F., & Narayan, R. 2022, MNRAS, 515, 2110
Shapley, H. 1928, Natur, 122, 482
Spitzer, L. 1969, ApJL, 158, L139
Tanner, A., Ghez, A. M., Morris, M., et al. 2002, ApJ, 575, 860
Tanner, A., Ghez, A. M., Morris, M. R., & Christou, J. C. 2005, ApJ, 624, 742
Tanner, A. M., Ghez, A. M., Morris, M., & Becklin, E. E. 2003, ANS, 324, 597
Viehmann, T., Eckart, A., Schödel, R., Pott, J. U., & Moultaka, J. 2006, ApJ,
  642, 861
Vollmer, B., & Duschl, W. J. 2000, NewA, 4, 581
von Fellenberg, S. D., Gillessen, S., Stadler, J., et al. 2022, ApJL, 932, L6
Wang, Q. D., Lu, F. J., & Gotthelf, E. V. 2006, MNRAS, 367, 937
Yelda, S., Ghez, A. M., Lu, J. R., et al. 2014, ApJ, 783, 131
Yusef-Zadeh, F., & Morris, M. 1991, ApJL, 371, L59
Yusef-Zadeh, F., Roberts, D. A., & Biretta, J. 1998, ApJL, 499, L159
Zajaček, M., Araudo, A., Karas, V., Czerny, B., & Eckart, A. 2020, ApJ,
  903, 140
Zhao, J.-H., Blundell, R., Moran, J. M., et al. 2010, ApJ, 723, 1097
Zhao, J.-H., Morris, M. R., Goss, W. M., & An, T. 2009, ApJ, 699, 186
Zhu, Z., Li, Z., Ciurlo, A., et al. 2020, ApJ, 897, 135
```